PASJ: Publ. Astron. Soc. Japan , 1–??,

Near Infrared Spectroscopy of M Dwarfs. I. CO Molecule as an Abundance Indicator of Carbon *

Takashi Tsuji
Institute of Astronomy, The University of Tokyo, 2-21-1 Osawa, Mitaka-shi, Tokyo, 181-0015
ttsuji@ioa.s.u-tokyo.ac.jp
and
Tadashi Nakajima
National Astronomical Observatory of Japan, 2-21-1 Osawa, Mitaka-shi, Tokyo, 181-8588
tadashi.nakajima@nao.ac.jp

(Received ; accepted)

Abstract

Based on the near infrared spectra of 42 M dwarfs, carbon abundances are determined from the rovibrational lines of CO 2-0 band. We apply $T_{\rm eff}$ values based on the angular diameters (15 objects) and on the infrared flux method (2 objects) or apply a simple new method using a $\log T_{\rm eff}$ (by the angular diameters and by the infrared flux method) – $M_{3.4}$ (the absolute magnitude at 3.4 μm based on the $WISE$ $W1$ flux and the Hipparcos parallax) relation to estimate $T_{\rm eff}$ values of objects for which angular diameters are unknown (25 objects). Also, we discuss briefly the HR diagram of low mass stars.

On the observed spectrum of the M dwarf, the continuum is depressed by the numerous weak lines of H_2O and only the depressed continuum or the pseudo-continuum can be seen. On the theoretical spectrum of the M dwarf, the true continuum can be evaluated easily but the pseudo-continuum can also be evaluated accurately thanks to the recent H_2O line database. Then spectroscopic analysis of the M dwarf can be done by referring to the pseudo-continua both on the observed and theoretical spectra. Since the basic principle of the spectroscopic analysis should be the same whether the true- or pseudo-continuum is referred to, the difficulty related to the continuum in cool stars can in principle be overcome. Although this procedure can easily be applied to the spectral synthesis method, we propose a simple method of analyzing EWs by taking the contamination of H_2O on CO lines into account: We measure the EWs of the CO blends (i.e., not necessarily limited to a single line) including H_2O as contamination and analyze them by the theoretical EWs evaluated from the synthetic spectrum including the effect of H_2O contamination as well.

In dense and cool photospheres of M dwarfs, almost all the carbon atoms are in stable CO molecules which remain almost unchanged for the changes of the physical condition in the photospheres. For this reason, the numerous CO lines can be excellent abundance indicators of carbon, and carbon abundances in late-type stars can best be determined in M dwarfs rather than in solar type stars. This somewhat unexpected advantage of M dwarfs in abundance analysis has not neessarily been recognized very well so far, but we determine carbon abundances rather easily to be $\log$ C/H between -3.9 and -3.1 in 42 M dwarfs. The resulting C/Fe ratios for most M dwarfs are nearly constant at about the solar value based on the classical high carbon abundance rather than on the recently revised lower value. This result implies that the solar carbon abundance is atypical for its metallicity among the stellar objects in the solar neighborhood if the downward revised carbon abundance is correct.

Key words: Molecular data — Stars : abundances — Stars : atmospheres — Stars : fundamental parameters — Stars : low mass

1. Introduction

M dwarf stars are the largest stellar group in the solar neighborhood. Also, because of their small masses, the lifetimes of M dwarfs are longer than the age of the Universe, and M dwarfs are composed of the samples of all the populations including very old ones. Unfortunately our understanding on this large and rich stellar group is rather poor compared to other stellar groups. This should largely be due to difficulty of observing M dwarfs because of their faintness, and the difficulty is most severe for the M dwarfs of the old population in the distant halo. Recent progress, however, overcame the observational barriers to some extent, especially in the field of stellar interferometry, infrared spectroscopy using new infrared detectors, astrometry and photometry from space, etc.

In addition to the faintness of M dwarfs, spectroscopic analysis of M dwarfs has also been hampered by the heavy blending of many atomic and molecular lines, especially in the optical region. This difficulty can be reduced somewhat in the infrared region, as has been shown by Mould

* Based on data collected at Subaru Telescope, which is operated by the National Astronomical Observatory of Japan.

(1978) who has carried out abundance analysis based on the near infrared spectra of six M dwarfs observed with the Fourier Transform Spectrometer (FTS) at KPNO. After this promising attempt in the 1970's, however, infrared spectroscopy of M dwarfs at high resolution could not be pursued further, because infrared detectors were not yet sensitive enough for faint M dwarfs. Recent progress of the infrared two-dimensional detectors finally made it possible to pursue spectroscopic analysis of M dwarfs further, as has already been demonstrated by Önehag et al. (2012) who have analyzed the infrared high resolution spectra in the J band region of about a dozen of M dwarfs.

Although spectroscopic analysis of the M dwarf star has been deemed difficult in general, we have some reasons why we study such a difficult case. For example, carbon and oxygen abundances in late-type stars are generally difficult to determine and their abundances are still controversial even for the Sun. This is because the abundance indicators of carbon such as the high excitation lines of neutral carbon and molecular lines such as of C_2 and CH (e.g., Grevesse et al. 1991; Asplund et al. 2005), for example, are mostly pretty model sensitive. In contrast, such a difficulty can be reduced in M dwarfs for which numerous lines of stable molecules such as CO and H_2O can be used as abundance indicators of carbon and oxygen, respectively. Such an advantage in the spectroscopic analysis of M dwarfs has not necessarily been well recognized so far and we hope to explore such a possibility in some detail in this paper.

Also, recent interests in M dwarfs come from possibilities to detect Earth-type planets around M dwarfs and to know the nature of such M dwarfs that host planets. Until the present, it has been suggested that metallicity of the planet hosting M dwarfs may be high (e.g., Johnson & Apps 2009). Also habitability of the planets may depend largely on their chemical environment and accurate abundance determination of the parent M dwarfs should be an important issue in investigating habitable planets themselves. However, direct abundance determinations in M dwarfs based on detailed spectroscopic analysis are still limited, and most estimations of metallicity were based on indirect methods based on low resolution spectroscopic or photometric indexes (e.g., Rojas-Ayala et al. 2012; Neves et al. 2013).

For extending detailed spectroscopic analysis to M dwarfs, however, another difficulty is the heavy veiling of the spectra by molecular bands, which obscures the true continuum needed to measure accurate line strengths (or equivalent widths). If we apply the spectral synthesis (SS) method, which has been more popular in recent years, the situation is the same, since the synthetic spectrum has usually been evaluated by referring to the true-continuum. Given that the problem of the continuum is a common feature that cannot be avoided in cool stars, we think that it is useful to examine the nature of the veil opacities in some details and reconsider such an analysis carried out by referring to the true-continuum. In fact, it is now possible to evaluate the pseudo-continuum level fairly accurately by virtue of the recent progress in molecular line database such as HITEMP2010 (Rothman et al. 2010) and many references cited therein (e.g., Barber et al. 2006). Then, we may abandon to refer to the true-continuum and reformulate the spectroscopic analysis in such a way as to proceed by referring to the pseudo-continuum defined by the molecular veil opacities. The basic principle of the spectroscopic analysis should be the same whether the true- or pseudo-continuum is referred to.

Now, the observational barriers are being overcome to some extent and the method of analysis can hopefully be improved somewhat as outlined above, we hope to pursue the possibility of determining accurate abundances directly from the observed spectra of M dwarfs.

In this paper, we first introduce our observed data (section 2) and then examine the necessary data and tools for spectroscopic analysis such as fundamental stellar parameters, model photospheres, and molecular data (section 3). We then carry out a preliminary analysis based on the conventional method disregarding the background opacity due to numerous H_2O lines (section 4), and consider the effect of H_2O contamination consistently in the analysis referring to the pseudo-continuum (section 5). Finally, we discuss some topics including method of analysis, carbon abundances in M dwarfs, accuracy of abundance analysis, and HR diagram at the end of the main sequence (section 6).

2. Observations

We observed 42 M dwarfs listed in the table 1, which were selected based on at least one of the following three criteria.

1. The distance of the target ($d < 30$ pc) is known by parallax measurements mostly by Hipparcos (van Leeuwen 2007). All the target stars satisfy this criterion.
2. The radius of the target star was obtained by interferometry (Boyajian et al. 2012, references therein). 16 stars whose names are marked by † in table 1 belong to this case.
3. The target star hosts a planet (or planets) (Marcy et al. 1998; Delfosse et al. 1998; Butler et al. 2004; Bonfils et al. 2005; Butler et al. 2006; Forveille et al. 2009; Johnson et al. 2010; Haghighipour et al. 2010; Apps et al. 2010; Howard et al. 2010; Forveille et al. 2011). Ten stars whose names are marked by ‡ in table 1 belong to this case.

Observations were carried out at the Subaru Telescope on 2013 May 9 and November 16 UT using the echelle mode of the Infrared Camera and Spectrograph (IRCS; Kobayashi et al. 2000) with natural guide star adaptive optics. The slit width of $0.14''$ was sampled at 55 mas pixel^{-1}, and the resolution was about 20000 at K. The echelle setting was "K^+", which covered about a half of the K window with the orders, wavelength segments and pixel-wise dispersions given in table 2. The targets were nodded along the slit, and observations were taken in ABBA sequence, where A and B stand for the first and second positions on the slit. Total exposure time

ranged from 24 seconds (GJ 820 A) to 54 minutes (GJ 3348 B). The night in May was photometric, while that in November was spectroscopic. Signal-to-noise ratios of reduced spectra at around 23000Å given in the fifth column of table 1, were typically higher for the run in May. At the beginning of the night in the May run and at the ending of the night in the November run, a rapidly rotating B8 star Regulus (α Leo) was observed as the calibrator of telluric transmission.

During the target acquisition by K band imaging, GJ 797 B was spatially resolved into an equal binary with a separation of $0.3''$ with NE and SW components. By placing the slit perpendicularly to the separation, each component was observed.

Data reduction was carried out using the standard IRAF[1] routines in the `imred` and `echelle` packages. After extraction of one dimensional spectra, wavelength calibrations were calculated using telluric absorption lines in the spectra of Regulus. After wavelength calibrations of one dimensional spectra of A and B positions, they were coadded to produce combined spectra. The combined spectra were normalized by the pseudo-continuum levels and then calibrated for telluric absorption using the spectra of Regulus.

table 1: Target stars (p.24).
table 2: Echelle setting (p.25).

3. Preparations for Spectroscopic Analysis

The basic parameters that characterize stellar spectra are effective temperature, surface gravity, chemical composition, and micro-turbulent velocity. However, it is difficult to determine all these parameters from the observed spectra, and it is helpful to obtain some of these parameters from other sources. We survey such a possibility especially in the recent stellar interferometry and in the databases based on space observations (subsection 3.1). With the basic parameters at hand, we generate model photospheres needed to compute theoretical spectra by which to analyze the observed spectra, and we briefly discuss our models (subsection 3.2). In the computation of the theoretical spectra, accurate molecular data are indispensable and we discuss the molecular data we are to use (subsection 3.3).

3.1. Fundamental Parameters of M Dwarfs

Thanks to the recent interferometric measurements of the angular diameters of M dwarfs, effective temperatures of dozens of M dwarfs are now known with sufficient accuracy (e.g., Boyajian et al. 2012) and about a third of our sample belong to this case. The problem is how to estimate effective temperatures of M dwarfs for which angular diameters are not known.. One possibility may be to apply photometric data, and the best way for this purpose may be to apply the infrared flux method (Blackwell et al. 1980). We applied this method by the use of the $L^{'}$ band flux but only to a limited number of M dwarfs (Tsuji et al. 1996). For extending this method to our M dwarfs, we looked for the $L^{'}$ band data in the literature, but we could not find them in the ground-based photometry for most of our sample. But we noticed that the $WISE$ $W1$ band flux centered at $3.4\,\mu$m (Wright et al. 2010) can be used for this purpose.

Meanwhile, however, we find it possible to use the $WISE$ data not in the infrared flux method but in another way: Namely, for M dwarfs for which interferometric $T_{\rm eff}$ values are available, we convert the $W1$ flux to the absolute magnitude at $3.4\,\mu$m, $M_{3.4}$, by the use of the Hipparcos parallax (van Leeuwen 2007). Then we use the resulting $M_{3.4} - \log T_{\rm eff}$ relation to infer $T_{\rm eff}$ from $M_{3.4}$ which is available for all the M dwarfs we are to analyze. There are 33 K and M dwarfs for which interferometrically determined $T_{\rm eff}$ are known with precision to better than 5% in table 6 of Boyajian et al. (2012). However, the $WISE$ fluxes were not resolved for the binary components GJ 338A, GJ 338B, GJ 702A, GJ 702B, GJ 820A, and GJ 820B, and we use the remaining 27 stars. To include later M dwarfs, we also consider nine M dwarfs whose $T_{\rm eff}$ values are determined by the infrared flux method (Tsuji et al. 1996). These 27 and 9 data are summarized in tables 3 and 4, respectively. For these 36 objects with known $T_{\rm eff}$, $M_{3.4}$ values are plotted against $\log T_{\rm eff}$ values in figure 1. Except for a few cases, $M_{3.4}$ and $\log T_{\rm eff}$ follow reasonably tight correlation and we draw a mean curve shown by the dashed line in figure 1.

The resulting $M_{3.4}$ - $\log T_{\rm eff}$ relation is used to estimate $T_{\rm eff}$ of M dwarfs for which $T_{\rm eff}$ values are not known. The resulting $T_{\rm eff}$ values together with $M_{3.4}$ values are given in table 5 for 25 M dwarfs. For two objects, GJ 273 and GJ 725B, which deviate from the mean relation in figure 1, we also estimate their $T_{\rm eff}$ values by using the $M_{3.4}$ - $\log T_{\rm eff}$ relation and the results are included in table 5. The resulting $T_{\rm eff} = 3415\,$K by the $M_{3.4}$-method is higher compared with $T_{\rm eff} = 3150\,$K (table 4) by the infrared flux method for GJ 273, while $T_{\rm eff} = 3337\,$K by the $M_{3.4}$-method is higher compared with the $T_{\rm eff} = 3104\,$K (table 3) by the interferometry for GJ 725B. We should in principle respect the results by the direct observations, but the consistency among all the data should be considered at the same time. We analyze the spectra of these two M dwarfs by the two different $T_{\rm eff}$ values - the high and low, and examine the overall consistency at the end (subsection 6.2). We attach H and L to the star names to discriminate the cases of high and low $T_{\rm eff}$, e.g., GJ 273-H and GJ 273-L.

In applying the $M_{3.4}$-method, the accuracy of the input data, especially of the $WISE$ photometry is most crucial. Generally, the major problem in the photometry of relatively bright objects is the possible saturation of the detectors. In this regard, the $WISE$ data quality has been

[1] IRAF is distributed by the National Optical Astronomy Observatory, which is operated by the Association of Universities for Research in Astronomy, Inc., under cooperative agreement with the National Science Foundation.

examined in detail by Avenhaus et al. (2012) who showed that the $W1$ band flux centered at 3.4 μm is of high quality and quite reliable. This is in marked contrast to the $W2$ band flux centered at 4.6 μm, which was showed to be not free from saturation effect and will result in significant errors for bright stars. By the way, Avenhaus et al. (2012) showed that there is no mid-infrared excess in about a hundred M dwarfs by the analysis of the $WISE$ data and concluded that there is no clear evidence for a debris disk around M dwarfs. This result implies that the visibilities measured by the interferometers are not likely to be disturbed by emission and/or scattering by the circumstellar dust. However, detailed analysis should be needed on deviating stars in figure 1 to see if such a conclusion can be applied to them.

We also plot $T_{\rm eff}$ values by different methods against the spectral types in figure 2. For this purpose, we find that 29 M dwarfs in our sample are included in 426 M dwarfs classified on a uniform system by Joy & Abt (1974) who used the strengths of TiO bands in the blue. As for remaining 13 M dwarfs, we apply the spectral types found in SIMBAD. Although these types due to different authors are naturally not on a uniform system, we confirm in our sample of 29 M dwarfs noted above that the SIMBAD types agree with those by Joy & Abt (1974) within 1 subtype for the 28 out of 29 M dwarfs and within 1.5 subtype for a remaining object GJ 205. Inspection of figure 2 reveals that the spectral type - $T_{\rm eff}$ relation is not defined very well, but most stars follow a mean relation (dashed line) with dispersion of $\pm$ 1 subtype (dotted lines)[2]. It is to be noted that there is little systematic effect among the $T_{\rm eff}$ values determined by the interferometry (filled circles), the infrared flux method (open circles), and the $M_{3.4}$-method (filled triangles).

The radii based on the angular diameters and masses mostly based on the mass-luminosity relations are also reproduced in 8- and 9-th columns, respectively, in table 3 from Boyajian et al. (2012). The $\log g$ values based on these radii and masses are given in the 10-th column of table 3, but only for those objects which are analyzed in the present paper. For the objects for which $T_{\rm eff}$ values are determined by the infrared flux method and by the $M_{3.4}$ - method, radii and masses are estimated by applying the empirical equations (8) and (10), respectively, given by Boyajian et al. (2012). The resulting values of $R/R_\odot$, $M/M_\odot$, and $\log g$ are given in the last three columns in tables 4 and 5 (but in table 4, only for objects which are analyzed in the present paper). Now, $T_{\rm eff}$ and $\log g$ values are ready for the 42 objects we are to analyze in this paper, and these data are plotted in figure 3 together with the result from the evolutionary models by Baraffe et al. (1998). Note that GJ 273 and GJ 725B appear twice for the different sources of $T_{\rm eff}$ values noted above. Also, GJ 273-L and, especially GJ 725B-L, show large deviations from other objects in figure 3.

[2] A large deviating star GJ 205 is very metal-rich and may be classified to be too late for its $T_{\rm eff}$. GJ 611B is metal poor and may be classified to be too early for its $T_{\rm eff}$. But we have no explanation for GJ 273-L, GJ 686, and GJ 725B-L.

figure 1: $M_{3.4}$ vs. $\log T_{\rm eff}$ (p.15).
figure 2: $T_{\rm eff}$ vs. Sp. types (p.16).
figure 3: $\log g$ vs. $T_{\rm eff}$ (p.16).

table 3: $T_{\rm eff}$ by the interferometry (p.25).
table 4: $T_{\rm eff}$ by the infrared flux method (p.26).
table 5: $T_{\rm eff}$ by $M_{3.4}$ – $\log T_{\rm eff}$ (p.27).

3.2. Model Photospheres of M Dwarfs

We apply the model photospheres of M dwarfs included as a part of our Unified Cloudy Models (UCM) (Tsuji 2002; 2005). Our present M dwarf sample is not so cool as to form dust clouds in their photospheres and we apply our dust free models for two abundance cases: *case a* (Ca-series) with the high C & O abundances ($\log A_{\rm C} = -3.40$ & $\log A_{\rm O} = -3.08$[3]) and *case c* (Cc-series) with the low C & O abundances ($\log A_{\rm C} = -3.61$ & $\log A_{\rm O} = -3.31$), which are based on the classical solar abundance (Anders & Grevesse 1989; Grevesse et al. 1991) and a downward revised solar one (Allende Prieto et al. 2002), respectively. Our grid covers $T_{\rm eff}$ between 700 and 4000K with a step of 100 K for $\log g = 4.5$, 5.0, and 5.5. However, inspection of tables $3 \sim 5$ reveals that $\log g$'s of most M dwarfs are somewhere between $\log g = 4.5$ and 5.0. For this reason, we generate an additional series of models with $\log g = 4.75$ ($T_{\rm eff} = 2600 \sim 4000$ K) in our UCM grid, and this series of models are used in the first iteration of our preliminary analysis (section 4).

However, we find that the abundance analysis is sensitive to the fundamental parameters, especially to $\log g$ (subsection 4.3). Then we finally decide not to use the models from our grid but to generate a specified model for $T_{\rm eff}$ and $\log g$ of each M dwarf, and use it in and after the second iterations. If the carbon abundance by our first iteration of the preliminary analysis appears to be closer to the classical solar abundance (or to the recent solar abundance), we apply the *case a* (or *case c*) abundance as the input C & O abundances for our models [4].

3.3. Molecular Data

The spectroscopic data of CO are relatively well known. Our CO data are based on the line position data (Guelachivili et al. 1983) and intensity data (Chackerian & Tipping 1983). Under the high density of the photospheres of M dwarfs, another important issue is the collision broadening, which depends on the physical properties of the interacting atoms or molecules. The collision half-width γ is relatively well studied for the collision partners

[3] $A_{\rm C}$ and $A_{\rm O}$ are the number densities of carbon and oxygen, respectively, relative to hydrogen. The abundances for *case a* including 34 elements are given in Table 1 of Tsuji (2002), and those for *case c* are the same as *case a* except for $A_{\rm C}$ and $A_{\rm O}$.

[4] We designate our model by cloud type/abundance case/$T_{\rm eff}$/$\log g$. For example, a model of no dust cloud (or clear model) with *case a* abundance, $T_{\rm eff} = 3360$ K, and $\log g = 4.85$ is referred to as Ca3360c485. As for details about our models of M, L, and T dwarfs, see an updated UCM database at http://www.mtk.ioa.s.u-tokyo.ac.jp/∼ttsuji/export/ucm2.

in the air (N_2, O_2...) at room temperature, but unfortunately not for collision partners in stellar photospheres (H, He, H_2...) at elevated temperatures. Usually, collision half-width γ is represented by

$$\gamma = \gamma_0 \frac{p}{p_0} (\frac{T_0}{T})^n, \quad (1)$$

where γ_0 is the collision half-width measured at a reference temperature T_0 (e.g. 296 K) and gas pressure p_0. The CO air-broadened values of γ_0 can be found in the CO database included in HITEMP2010 (Rothman et al. 2010), but those by molecular hydrogen appropriate for temperatures as high as 3000 K are available only for CO pure rotation transitions (Faure et al. 2013) so far as we are aware. As an example of the effect of the collision partner, we compare the H_2 broadening half-widths (converting from MHz/Torr to cm^{-1}/atm unit from Faure et al. (2013)) and air-broadening ones (Rothman et al. 2010) for the case of CO pure rotation transitions in table 6.

Inspection of table 6 reveals that the effect of collision partners is rather small in the low J transitions but quite appreciable in the high J transitions. The values of γ_0 for the air-broadening of CO 2-0 vibration-rotation transitions which we analyze in this paper are rather similar (Rothman et al. 2010) to the case of the pure rotation transitions shown in table 6. Although it is possible that the H_2-broadening is about 50 % larger than the air-broadening, we apply the medium value of $\gamma_0 = 0.05\,cm^{-1}$/atm for the air-broadening data (Rothman et al. 2010) to all the CO 2-0 lines we study in this paper ($J \approx 30 - 70$). We hope that measurements of the H_2-broadening at high temperatures can be extended to the vibration-rotation transitions of CO in the near future.

For the reason to be noted in subsection 4.1, we decide to concentrate to the CO lines near the (2,0) bandhead region and select CO blends listed in table 7 in which the spectroscopic data of CO lines are given. We hoped that this spectral region may be relatively free from other molecular bands. In fact, our line-list includes some lines of CN Red System, ro-vibrational lines of OH, HF, H_2 etc., but none of these molecular lines is prominent in the region we are to study. However, we notice that the wings of H_2O ν_1 and ν_3 bands centered at 2.7 μm and $\nu_2 + \nu_3$ band centered at 1.87 μm extend to the region of the CO 2-0 band and numerous weak H_2O lines produce appreciable effect on the continuum level. Also some CO lines are blended with the H_2O lines in such a way that their equivalent widths are modified by the blends.

We first examine the effect of H_2O lines with the use of the line-list by Partridge & Schwenke (1997) on a model of Cc3500c50 and $\xi_{\rm micro} = 1\,{\rm km\,sec^{-1}}$. The result is shown in figure 4a in which the predicted spectrum with the resolution of about 10^5 is shown by the thin line and that convolved with the slit-function (Gaussian) with FWHM = 16 km sec^{-1} (the resolution of our observed spectra) by thick line. Next, we do the same but with the use of a new water line-list in HITEMP2010 (Rothman et al. 2010) which has extensively used the BT2 database by Barber et al. (2006) (figure 4b). Although the general patterns of the H_2O spectra in figures 4a and 4b are not very different, the depressions of the continua are much larger in figure 4b (more than 3 %) than in figure 4a (less than 1 %). For comparison, the predicted spectrum of CO alone shows the continuum clearly (figure 4c). Although the collision half-widths of H_2O lines span the larger range compared with those of CO, we apply the same mean value as for CO for H_2O lines in which the damping wings are not yet developed.

The number of H_2O lines with cut-off at the integrated intensity [5] of $S(T = 2500\,{\rm K}) \approx 3 \times 10^{-27}\,{\rm cm\,molecule^{-1}}$ in the spectral region shown in figure 4 (22925 - 23020 Å) is 3021 by the line-list of Partridge & Schwenke (1997) while it is 32970 by BT2-HITEMP2010. The number of lines in the original BT2-HITEMP2010 database is still several times larger. This large increase is due to inclusion of many weak lines in BT2-HITEMP2010, and it is such numerous weak lines that play important role in depressing the continuum level noted in figure 4b. Also, with such a high line density of about 350 lines per 1 Å interval for the cut-off noted above, the H_2O opacity should be smeared out and the pseudo-continuum can be well defined at nearly constant level as shown in figure 4b. For this reason, spectral analysis can be carried out by referring to the pseudo-continuum instead of the true-continuum, as will be discussed in section 5.

---

figure 4a,b,c: Theoretical spectra of H_2O and CO (p.17).

table 6: Effect of collision partners on γ (p.27).
table 7: Spectroscopic data of the CO lines (p.28).

---

4. A Preliminary Analysis

We first examine the CO spectra (subsection 4.1) and apply a usual method of abundance analysis to the CO lines without considering the possible effect of the blending of the H_2O lines (subsection 4.2). The external errors due to the uncertainties in the fundamental parameters including the overall metallicity are discussed (subsection 4.3).

4.1. CO Lines

In this paper , we focus our attention to the lines of the CO first-overtone band. Although CO lines are clearly observed in the spectral region observed, most lines are blends of two or more CO lines in our medium resolution spectra of $R \approx 20000$ (figure 4c). Also, we notice that H_2O lines are already disturbing the region of the CO first overtone band. As can be inferred from figure 4b, numerous weak H_2O lines depress the continuum level on one hand and some relatively strong H_2O lines disturb the individual CO lines as blends on the other. All these facts make it difficult to measure equivalent widths accurately

[5] line absorption cross-section[cm^2] integrated in the wavenumber [cm^{-1}] space over the entire line profile.

and, in particular, it is very difficult to measure weak lines.

We first hoped to measure as many CO lines as possible recorded in our echelle spectra since it is essential to include weak unsaturated lines and saturated stronger lines together to determine micro-turbulent velocity, which is the important parameter next to the effective temperature and gravity in the interpretation of stellar spectra. However, the situation noted above, namely blending of CO lines themselves, blending of H_2O lines disturbing both continuum level and CO line strength, and difficulty to measure weak CO lines, makes it difficult to determine micro-turbulent velocity spectroscopically. On the other hand, the micro-turbulent velocity in the photosphere of M dwarfs may be less than 1 km sec^{-1} (e.g., Bean et al. 2006) while the thermal velocity of CO is 1.33 km sec^{-1} for $T \approx 3000$ K. Then the role of the micro-turbulence in the line-broadening in the photospheres of M dwarfs may not be so important as in M giant stars in which the micro-turbulent velocity is larger than 1 km sec^{-1}. For this reason, we give up to determine the micro-turbulent velocity spectroscopically in our M dwarfs and assume it to be 1 km sec^{-1} throughout this paper.

Once we give up to determine the micro-turbulent velocity, it is almost useless to measure many CO lines which are more or less disturbed by various noises, and we focus our attention to the CO (2-0) bandhead region shown in figure 4c. In this region, the effects of H_2O ν_1 and ν_3 bands are relatively small compared to the longer wavelength region and there is no overlapping of various CO bands. We then concentrate to determine carbon abundance from the restricted CO features listed in table 7.

4.2. Analysis by Blend-by-Blend

All the CO lines we are to analyze are blends of two CO lines on our medium resolution spectra (figure 4c). In such a case, the usual curve-of-growth method cannot be applied. Instead, spectral synthesis (SS) method may be considered, since it is possible to treat the blended features easily by this method. However, SS method has been applied so far only when the true-continuum could have been defined and, for this reason, it may be difficult to apply to M dwarfs for which the true-continuum cannot be defined in general. Although we hope to relax this difficulty as will be detailed in section 5, we here extend the line-by-line (LL) method extensively applied to the unblended lines in red giant stars (e.g., Tsuji 2008) to the case of blended lines in M dwarfs and now the method should better be referred to as the blend-by-blend (BB) method.

We measure the equivalent widths (EWs) of the blends composed of two CO lines listed in table 7, and the results are given in table S1[6]. Now the problem is to determine the carbon abundance from these EWs. Since almost all the carbon atoms are in CO molecules in the photosphere of M dwarfs, the carbon abundance is almost the same as the CO abundance. However, it is not possible to obtain CO and hence carbon abundances directly from the measured EWs. But the reverse is possible; i.e., determine directly the EW of a CO blend for a given carbon abundance. Then, we start from the carbon abundance $\log A_{\rm C}^{(0)}$ of the model photosphere used (i.e., $\log A_{\rm C}^{(0)} = -3.61$ for our models of Cc-series) and compute the EW of a CO blend. If the resulting EW is smaller than the observed EW, the assumed carbon abundance should be too small. We then compute EWs, $W(\delta)$, for the logarithmic abundance corrections of $\Delta\log A_{\rm C} = \delta = +0.3$ and $+0.6$, and we have so to speak a mini curve-of-growth for the CO blends defined by $\log W(\delta)/\lambda$ vs. δ (δ = 0.0, 0.3, and 0.6). With this mini curve-of-growth, the abundance correction to the initial value of $\log A_{\rm C}^{(0)} = -3.61$ can be obtained from the observed EW of the CO blend. This process is repeated to all the CO blends listed in table 7 except for the lines of Ref. nos. 13 and 14 which appear to be badly blended with H_2O lines, and the mean of the resulting abundance corrections for about a dozen of the CO blends is obtained.

An example of the above noted procedures is shown in figure 5a for the case of GJ 412A: The ordinate is the logarithmic abundance correction obtained from the observed equivalent width indicated by the abscissa. The resulting mean correction $\Delta\log A_{\rm C}^{(1)}$ = -0.18 is shown by the dashed line, and the result indicates that the carbon abundance should be lower in GJ 412A than in the value assumed. The revised logarithmic carbon abundance is obtained by

$$\log A_{\rm C}^{(1)} = \log A_{\rm C}^{(0)} + \Delta\log A_{\rm C}^{(1)}. \qquad (2)$$

Another example is shown in figure 6a for HIP57050 which appears to be very carbon rich (about 3 times larger compared to the initial solar value). Also, the case of the coolest object GJ 406 is shown in figure 7a. The results for our 42 M dwarfs are summarized in table 8 in which object identification, $T_{\rm eff}$, $\log g$, model photosphere used in the first iteration, the logarithmic carbon abundance correction $\Delta\log A_{\rm C}^{(1)}$, and the resulting logarithmic carbon abundance $\log A_{\rm C}^{(1)}$ are given through first to 6-th columns.

Now we have a rough idea on the carbon abundance for each M dwarf and we proceed to the second iteration, in which we apply our models of Ca or Cc series depending on whether $\log A_{\rm C}^{(1)} \gtrsim -3.50$ or < -3.50. We also use the model specified for $T_{\rm eff}$ and $\log g$ of each object instead of the model from our UCM grid. We then assume the carbon abundance resulted from the first iteration as an input value and the same procedure as for the first iteration is repeated. Some examples of this process are shown in figures 5b, 6b, and 7b for GJ 412A, HIP 57050, and GJ 406, respectively. The resulting second logarithmic abundance corrections shown by the dashed lines in figures 5b, 6b, and 7b are still non-zero but rather small in all the three cases. The results for 42 M dwarfs are summarized in table 8, in which the specified model photosphere used, the second logarithmic abundance correction $\Delta\log A_{\rm C}^{(2)}$, and the resulting logarithmic carbon abundance

[6] This table is available only in the electronic version as a supplementary data. Note that the line of Ref. no. 11 is not measured because this line is blended with Sc I line and hence not used in our analysis.

$$\log A_{\rm C}^{(2)} = \log A_{\rm C}^{(1)} + \Delta\log A_{\rm C}^{(2)}, \quad (3)$$

are given in 7-th, 8-th, and 9-th columns, respectively.

Finally, we repeat the same procedure starting from the new logarithmic carbon abundance $\log A_{\rm C}^{(2)}$ and confirm that the resulting correction is almost null as shown in figures 5c, 6c, and 7c for GJ 412A, HIP 57050, and GJ 406, respectively, confirming that our preliminary analysis by the BB method has converged.

figure 5: Blend-by-blend (BB) analysis of GJ412A (p.17).

figure 6: BB analysis of HIP 57050 (p.18).

figure 7: BB analysis of GJ406 (p.18).

table S1: EWs of CO blends (for electronic version) (table 14 in p.33).

table 8: The result of the BB analysis for 42 M dwarfs (p.29).

4.3. External Errors

Besides the internal errors (probable errors) of the BB analysis mostly 0.05 - 0.10 dex (table 8), there are various sources of the external errors. We here examine the errors due to the uncertainties of the fundamental parameters. For this purpose, we select three objects representing early (GJ 338A; dM0.5), middle (GJ 436; dM3.5), and late (GJ 406; dM6.5e) M dwarfs, and repeat the BB analysis for the reference parameters, which we think to be close to the best solution for each object, by the use of the appropriate model for the parameters (first line for each star in table 9). The resulting logarithmic abundance correction $\Delta\log A_{\rm C}$ to the assumed initial value (given in the parenthesis in the first column) is given in the 5-th column. Then, we change $T_{\rm eff}$ by $\pm$50 K (second & third lines for each object), $\log g$ by $\pm$0.25 (4- & 5-th lines), and $\xi_{\rm micro}$ by $\pm0.5\,{\rm km\,sec^{-1}}$ (6- & 7-th lines) from those of the reference model, and carry out the BB analysis by the use of the appropriate model for the changed parameter. The resulting logarithmic abundance correction and the difference from that for the reference model are given in the 5-th and 6-th columns respectively, in table 9 for each object. We also examine the effect of changing the Cc-series, which we are using throughout the seven cases so far, to the Ca-series with the fundamental parameters of the reference model in the first line for each object (8-th line for each object in table 9).

Inspection of table 9 reveals that uncertainties of $\pm$50 K in $T_{\rm eff}$ result in rather modest effects smaller than (in early M) or comparable with (late M dwarf) the internal errors. This result can be understood if we remember that CO formation is already complete (i.e., almost all the carbon is in CO) and hence its abundance remains almost unchanged for the changes of temperatures. On the other hand, uncertainties of $\pm$0.25 dex in $\log g$ result in an appreciable effect especially in earlier M dwarfs. This may reflect the pressure dependence of the background opacities due to the $f-f$ transitions of H^- and H_2^- and collision-induced dipole transitions of H_2, which are larger at higher gravity and hence require a positive abundance correction (i.e. larger carbon abundance). In the late M dwarf GJ 406, CO lines are pretty strong (see figure 13) and larger pressure broadening under the higher gravity may require negative abundance correction (i.e. smaller carbon abundance is sufficient to account for the observed EWs). The uncertainties of $\pm0.5\,{\rm km\,sec^{-1}}$ in the micro-turbulent velocity $\xi_{\rm micro}$ result in considerable changes in the carbon abundances. This result implies that the problem of the micro-turbulent velocity remains to be important even in the spectral analysis of M dwarfs in which the pressure broadening plays significant role. We could not determine the micro-turbulent velocity in this study, and this is the major shortcoming that we hope to conquer in the near future. Finally, larger C & O abundances in the Ca-series compared to the Cc-series result in higher temperatures in the photosphere due to the increased line blanketing effect, and hence have a similar effect as the increased $T_{\rm eff}$ (compare the third and 8-th lines in each object in table 8).

Another source of external error is the overall metallicity which we assumed to be the solar for all the models. As an example of low metallicity case, we examine GJ412A which shows a large decrease of carbon ($\Delta\log A_{\rm C}$ = -0.181; table 9). For this purpose, we generate a model in which all the metal abundances are reduced by 0.20 dex from the solar and repeat the BB analysis with the resulting model. The result shown in the last line in table 9 suggests that the uncertainty due to the use of solar metallicity model is 0.094 dex. The effect of the reduced metallicity on the thermal structure of the model is a decrease of temperatures due to the less efficient backwarming effect and has a similar effect as the case of the decreased $T_{\rm eff}$.

table 9: Effect of the external errors on abundance determinations (p.30).

5. Analysis of the Spectra with the Depressed Continua by the Molecular Veil Opacities

In the observed spectrum, we measure CO lines by referring to the pseudo-continuum, but analyzed the observed equivalent width measured in this way by the use of the predicted one evaluated by referring to the true continuum (subsection 4.2). This analysis is obviously not self-consistent. As a possibility to resolve such inconsistency, we analyze the spectra by referring to the pseudo-continua both in observed and predicted spectra (subsection 5.1). We then consider the effect of the contamination of weak H_2O lines in the computation of the predicted EWs, with which we analyze the observed EWs including the blending of weak H_2O lines as well. In this way, the consistency of the analysis can be recovered (subsection 5.2). Finally, we examine the results by the spectral synthesis and χ^2-test (subsection 5.3).

5.1. *Effect of the H_2O Veil Opacity on the Continua*

To examine the results of the BB analysis outlined in section 4, the spectral synthesis (SS) method can be of some use. For this purpose, we first show a theoretical spectrum of the CO (2-0) bandhead region for our model Cc2800c517 applied to GJ 406 in figure 8a. The spectrum is first calculated at the sampling interval of 0.02 Å or $R \approx 10^{+5}$ (thin line) and then convolved with the slit function of the spectrograph (Gaussian) with FWHM = 16 km sec^{-1} (thick line). Hereafter, we always show this low resolution version of the theoretical spectrum alone for simplicity throughout this paper. In the predicted spectrum, the true continuum level is obviously known but cannot be seen at all in figure 8a, and we know from figure 4b that this is entirely due to numerous weak lines of H_2O. However, the upper envelope of the spectrum can be well defined as shown by the dashed line, as we already know in the case of H_2O lines alone in figure 4b. This means that the pseudo-continuum level can be well defined even though the "continuum" level is depressed by about 8% for the low resolution spectrum.

In the observed spectra of M dwarfs, it is only possible to draw a pseudo-continuum. Given that it is possible to define the pseudo-continuum accurately in the predicted spectrum as in figure 8a, we can compare the observed and predicted spectra both normalized by their pseudo-continua. Thus we renormalize the predicted spectrum in figure 8a by its pseudo- continuum (dashed line in figure 8a) and the result is shown in figure 8b (thick line) in comparison with the observed spectrum also normalized by its pseudo-continuum (filled circles) [7]. The observed (filled circles) and predicted (thick line) spectra both normalized by their pseudo-continua show a reasonable match, but the observed spectrum cannot be matched at all with the predicted spectrum normalized by its true continuum (simply copied from figure 8a above but shown by thin line). Hereafter, we always compare the observed and predicted spectra, both normalized by their pseudo-continua.

In the comparison outlined above, we assume $\log A_C$(BB) = -3.55 (table 8) for GJ 406 and $\log A_O = \log A_C + 0.30$. The effect of oxygen abundance on CO spectrum may not be important since CO abundance is almost determined by the carbon abundance alone. However, if carbon abundance turns to be very large in some M dwarfs and if oxygen abundance is kept at its initial solar value, then it may happen that $A_C > A_O$ or the M dwarf turns to the dwarf carbon star! To prevent such a catastrophe, we always adjust the oxygen abundance to be $A_O/A_C = 2.0$ for the given carbon abundance throughout this paper. It is to be noted that this O/C ratio is assumed to be the same as the solar value (e.g.. Allende Prieto et al. 2002).

Now, as examples of comparing the observed and predicted spectra this way, we show the cases of GJ 412A and HIP 57050 in figures 9a and 9b, respectively. The thick lines are predicted spectra for the final carbon abundances of our BB analysis, $\log A_C^{(2)}$, and the thin lines for $\log A_C^{(2)} \pm \delta (= 0.3)$. The observed spectra normalized by their pseudo-continua (shown by the filled circles) appear to agree rather well with those predicted for $\log A_C^{(2)}$ (thick lines). We also evaluate χ^2 values by

$$\chi^2 = \frac{1}{N-1} \sum_{i=1}^{N} \left(\frac{f^i_{\rm obs} - f^i_{\rm cal}}{\sigma_i} \right)^2, \qquad (4)$$

where $f^i_{\rm obs}$ and $f^i_{\rm cal}$ are observed and predicted spectra normalized by their pseudo-continua, respectively. N is the number of data points and σ_i is the noise level estimated from the S/N ratio in table 1 (assumed to be independent of i). Resulting χ^2 values for GJ 412A are 7.719, 4.241, and 17.469 for δ = -0.3, 0.0, and +0.3, respectively, where δ is a modification applied to $\log A_C^{(2)}$. For HIP 57050, χ^2 values are 8.070, 3.808, and 11.520 for δ = -0.3, 0.0, and +0.3, respectively. The χ^2 values for $\log A_C^{(2)}$ of 42 M dwarfs are given in the 10-th column of table 8. In evaluating χ^2 values, some spectral regions dominated by absorption other than CO are masked (shown by the filled areas in figures 8, 9, and 13).

We must remember that our logarithmic carbon abundances $\log A_C^{(2)}$ themselves are determined without considering the effect of the H_2O contamination (subsection4.2). Nevertheless, the fittings of the observed and predicted spectra, both normalized by the pseudo-continua defined by the numerous weak H_2O lines, appear to be not so bad, and this may be simply because the depressions of the continua by the H_2O blends are not very large [8]. But we should consider the effect of the H_2O contamination in the determination of the carbon abundance itself and we discuss this problem next in subsection 5.2.

---

figure 8a,b: Observed and predicted spectra of GJ 406 (p.19).

figure 9a,b: Observed and predicted spectra of GJ 412A and HIP 57050 (p.19).

---

[7] Hopefully the pseudo-continua for the observed and predicted spectra can be drawn consistently. Practically, pseudo-continuum for the predicted spectrum for a short interval can be a straight line passing through the highest peak and hence rather simple. On the other hand, the case of the observed spectrum may not be so simple since the pseudo-continuum level may suffer the effect of the variations due to the atmospheric transmission, atmospheric absorption, detector sensitivity etc. Of course, these effects are corrected for during the data reductions, but some effects may remain uncorrected. Thus, the problem of the reference "continuum" is still a troublesome problem even by the use of the pseudo-continuum.

[8] The depressions of the continua of the predicted spectra are about 1, 3, 6, and 8 % for the models of $T_{\rm eff}$ = 3800, 3500 (see figure 4b), 3200, and 2800 (see figure 8a) K, respectively, but depend also on $\log g$ (for example, about 10 % for slightly higher gravity in $T_{\rm eff}$ = 2800 K model). The amount of the depression can be known only for the theoretical spectrum and never be known for the observed spectrum, since the true-continuum level cannot be known.

5.2. Blend-by-Blend Analysis Based on the Equivalent-Widths Measured on the Synthetic Spectra

One method to take the effect of H_2O contamination in determination of the carbon abundances based on CO analysis may be to apply the SS method, which is now possible to apply to the spectra whose true-continua cannot be seen, by the way outlined in the preceding subsection. We have already computed the spectra for three values of carbon abundances in subsection 5.1 and applied the χ^2-test for the fitting of the predicted spectra to the observed spectrum. Just by computations of additional several spectra with their χ^2 values, carbon abundance can be obtained by minimization of the χ^2 values. However, the SS method seems to be a bit too intricate especially for our medium resolution spectra. In fact, there is little merit to apply such a method to medium resolution spectra blurred by the slit function of FWHM as large as 16 km sec^{-1}, which washes out all the details of the spectra characterized by the velocity parameters (micro- and macro-turbulence, rotation etc.) generally smaller than 1 km sec^{-1}. Moreover, the SS method is by no means not free from its own limitations as will be discussed later (subsection 6.1). For these reasons, we propose a more simple method based on the equivalent width measurements instead.

For this purpose, we proceed as in our preliminary analysis (subsection 4.2) but the predicted equivalent widths (EWs) are calculated by including the effect of H_2O contamination and by referring to the pseudo-continuum instead of the true-continuum. This can be done in principle by using the usual code of evaluating the EWs, but it is again a bit too intricate to include thousands of weak H_2O lines in computing an EW of a CO blend, by referring to the pseudo-continuum which is difficult to know locally instead of the true-continuum which is obvious in the theoretical spectrum. Instead we can proceed more easily by measuring the EWs on the synthetic spectrum in the same way as we measure the EWs on the observed spectrum. In this way, the effect of the H_2O contamination can be taken into account automatically and the pseudo-continua can also be defined consistently for the predicted and observed spectra.

Actually, we calculate the synthetic spectra for $\log A_{\mathrm{C}}^{(2)}$ in 9-th column of table 8 and $\log A_{\mathrm{C}}^{(2)} \pm \delta$ (some examples for the case of $\delta = 0.3$ is shown in figures 8a and 8b), and we measure the predicted EWs, $W(\delta)$, for the CO blends listed in table 7. We now include the lines of Ref. no. 13 and 14, since the effect of the H_2O blending can be corrected for, but we exclude the line of Ref. no. 1 which appears to be too close to the bandhead. Then we have mini curves-of-growth defined by $W(\delta)/\lambda$ vs. δ (e.g. δ =-0.3, 0.0, and +0.3), by which the logarithmic abundance corrections to $\log A_{\mathrm{C}}^{(2)}$ required to explain the observed EWs can be obtained. We assume $\delta = \pm 0.3$ at the beginning. However, we find that the logarithmic abundance corrections do not exceed -0.1 in general. Then, we assume $\delta = -0.1$ and a linear interpolation is sufficient to find the abundance correction for each observed EW. Thus our final blend-by-blend analysis based on the EWs measured on the synthetic spectra (to be referred to as BBSS or simply as BS method) is quite simple.

As an example of the BS analysis, the resulting logarithmic abundance corrections for the case of GJ 412A are shown in figure 10 against the observed EWs used, and we obtain the mean value of $\Delta\log A_{\mathrm{C}}^{(3)} = -0.09 \pm 0.04$ shown by the dashed line. This is the correction to the carbon abundance obtained from CO blends disregarding the effect of H_2O contamination in table 8, and our iterative abundance analysis now finishes by this self-consistent analysis taking the effect of H_2O blending into account. The resulting final logarithmic carbon abundance is:

$$\log A_{\mathrm{C}}^{(3)} = \log A_{\mathrm{C}}^{(2)} + \Delta\log A_{\mathrm{C}}^{(3)}. \qquad (5)$$

Additional examples are shown in figures 11 and 12 for HIP 57050 and GJ 406, respectively. We carried out this analysis for our 42 M dwarfs and the resulting logarithmic abundance corrections and the final logarithmic carbon abundances with the probable errors are given in the second and third columns of table 10, respectively. It is to be noted that the values of $\Delta\log A_{\mathrm{C}}^{(3)}$ are always negative for 42 M dwarfs, and this is because the carbon abundances overestimated by the BB analysis neglecting the effect of contamination of H_2O lines are now corrected for by the BS analysis taking this effect into account.

Inspection of figures 5 $\sim$ 7 reveals that the abundance corrections by the BB analysis always increase with the observed EWs. Normally, the variations of the abundance corrections plotted against the EWs used provide important information on the physical parameters relating to the line formation such as the micro-turbulent velocity (e.g., Tsuji 2008). In the present case, however, the lines used are confined to a restricted intensity range and the variations may simply be explained as the effect of contamination mainly of H_2O lines. In fact, EW will increase by the blend of H_2O lines and a larger EW naturally results in a larger abundance correction, exactly as shown in figures 5 $\sim$ 7. This systematic effect disappears in figures 10 $\sim$ 12 where the effect of H_2O contamination is properly considered. Also, the abundance corrections, after the effect of H_2O contamination is corrected, approach the lowest abundance corrections in figures 5 $\sim$ 7 obtained by disregarding the H_2O blending. This may be because such lines giving the lowest abundance corrections in figures 5 $\sim$ 7 are simply those suffer least effect of H_2O contamination.

---

figure 10: Blend-by-blend analysis by EWs measured on synthetic spectrum (BS method) of GJ 412A (p.20).

figure 11: BS analysis of HIP 57050 (p.20).

figure 12: BS analysis of GJ 406 (p.20).

table 10: The result of BS analysis for 42 M dwarfs (p.31).

5.3. Final Check by the Spectral Synthesis and χ^2-Test

We generate the synthetic spectra for our final logarithmic carbon abundances $\log A_{\rm C}^{(3)}$ in table 10 and assuming the logarithmic oxygen abundances of $\log A_{\rm O} = \log A_{\rm C}^{(3)} + 0.30$. We compare the observed (filled circles) and predicted (solid line) spectra for six M dwarfs in figure 13 and the fits are generally fine if not perfect. Inspection of figure 13 reveals that the change of the observed spectra from dM0 to dM6.5 can be well accounted for by the predicted spectra with $T_{\rm eff} \approx 2800 \sim 3900$ K and $\log A_{\rm C} \approx -3.8 \sim -3.2$. By the way, a feature at $\lambda \approx 22970$ Å was identified as due to Ti I a ^{3}G$_5$ - z ^{3}F$_4$ and a blending feature at $\lambda \approx 22973$ Å to Sc I a ^{4}F$_{9/2}$ - z ^{4}F$^0_{9/2}$ on the sunspot umbral spectrum (Wallace & Livingston 1992). The H_2O feature just shortward of the CO (2, 0) bandhead strengthens towards later M dwarfs as expected.

For GJ 412A and HIP 57050, we can compare figures 13c and 13d with figures 9a and 9b, respectively, showing the similar comparisons but with the results of the BB analysis. The differences are rather minor, but the improvements can be confirmed by their χ^2 values (see below). The χ^2 values for the final abundances $\log A_{\rm C}^{(3)}$ by the BS analysis are given in 4-th column of table. 10 for the 42 M dwarfs, and the results show definite improvements compared with those for the abundances $\log A_{\rm C}^{(2)}$ by the BB analysis given in the 9-th column of table 8 in general.

Finally, we evaluate the χ^2 values for the synthetic spectra assuming several carbon abundances and plot the results against the assumed logarithmic carbon abundances in figure 14 for three M dwarfs, GJ 412A, GJ 406, and HIP 57050. The points marked by $\pm n\delta$ ($\delta = 0.1; n = 1-3$) are χ^2 values for the synthetic spectrum assuming $\log A_{\rm C} = \log A_{\rm C}^{(2)} \pm n\delta$ with $\log A_{\rm C}^{(2)}$ for each object given in the 9-th column of table 8. The points marked by BB are χ^2 values for our final carbon abundances of the BB analysis while those by BS for our BS analysis. Inspection of figure 14 reveals that our BS analysis results in the χ^2 value near the minimum for each object. Thus our simple BS analysis results in almost the same carbon abundance as by the minimization of χ^2 values.

---

figure 13: Predicted vs. observed spectra for 6 M dwarfs (p.21).

figure 14: χ^2-test for GJ412A, GJ406, and HIP 57050 (p.22).

---

6. Discussion

6.1. Method of Analysis

The major obstacle in the abundance analysis of cool stars has been the difficulty to locate the continuum level, and this problem is not limited to M dwarfs but has been a serious problem in cool luminous stars including M giant and supergiant stars. We hope to relax this difficulty by analyzing the spectra by referring to the pseudo-continuum instead of the true-continuum. Certainly, the pseudo-continuum defined by the collective effect of numerous weak lines is much more complicated compared with the true-continuum defined by the free-free or bound-free transitions of a few atoms and ions. However, the spectroscopic analysis can be carried out essentially the same way by referring to the pseudo-continuum instead of the true-continuum. For example, we measure EWs of the blended features by referring to the pseudo-continuum both in the observed and predicted spectra. Then, the analysis of EWs can be carried out as usual and this is important since the analysis of EWs plays a significant role in the spectral analysis for the reason to be noted below.

In the analysis of the complicated spectra composed of many blended lines, the spectral synthesis (SS) method has been widely employed, and the best fit has been determined by the χ^2-test in general. However, an important drawback in this approach is that the different line broadenings could not be separated well. Especially, the micro-turbulent velocity could not be determined well since its effect could not be separated from those of macro-turbulence and rotation on the synthetic spectrum. For example, the SS method was applied to several M dwarfs and micro- and macro-turbulent velocities were determined by Bean et al. (2006) , but it is not very clear how these two velocities could have been separated. Also, many groups used the SS method in a comparative study of the spectra of cool giant stars but the turbulent velocities were not determined well in many cases by the SS method (Lebzelter et al. 2012).

The important discovery of the micro-turbulent velocity was done from the analysis of the equivalent widths by the curve-of-growth method (Struve & Elvey 1934), and it is the EWs that are directly influenced by the micro-turbulent velocity. On the other hand, other line broadenings such as due to the macro-turbulence and rotation give no effect on EWs and they are recognized only on the synthetic spectrum. For this reason, the micro-turbulent velocity can be determined accurately and easily from the analysis of EWs, as has been shown for the case of cool giant stars (e.g., Tsuji 2008; 2009). Once the micro-turbulent velocity is determined, then the SS method can be used to infer the effect of the additional broadenings such as the macro-turbulence and rotation. Certainly, SS method is not useful as a means by which to determine all the parameters but it can be useful to check the overall consistency at the end.

At the beginning of this study, we hoped to determine the micro-turbulent velocity first from the analysis of EWs by the LL method, but this attempt could not be realized with the medium resolution spectra at hand (subsection 4.1). Even with the higher resolution, the effect of the blending makes the LL method difficult. For this purpose, we propose to analyze the EWs measured on the synthetic spectra in subsection 5.2 and this method, referred to as BS method, works well in determining the abundance. By this method, analysis of EWs is not necessarily limited to single lines but can be extended to blended lines found in the region of depressed continua. We hope to apply this

method to determining the micro-turbulent velocity with the higher resolution spectra. This is certainly a more challenging problem, but this should be almost unique way to determine the micro-turbulent velocity in the M dwarf photospheres.

6.2. Carbon Abundances in M Dwarfs

Determination of carbon abundances in late-type stars has been difficult in general and we do not yet have a result generally accepted even for the Sun. This is because the spectral lines used as indicators of carbon abundance are highly sensitive not only to the thermal structure of the photosphere but also to the inhomogeneity and non-LTE effects etc. In contrast, such difficulties can be avoided in M dwarfs for which CO molecule can be used as the abundance indicator. In the cool and dense photospheres of M dwarfs, almost all the carbon is in CO and hence its abundance shows little change for the changes of the physical condition. This advantage cannot be applied to hotter stars such as the Sun, in which CO formation is not yet complete but changes its abundance drastically for a minor change of temperature[9]. For this reason, CO cannot be a good abundance indicator of carbon for the Sun (Tsuji 1977). Despite such a difficulty, however, an extensive analysis on the solar model photoshpere with the use of CO spectrum itself has been done and the solar carbon, oxygen, and their isotopic abundances have been determined from the CO ro-vibrational spectrum (Ayres et al. 2006).

Given that the difficulty due to the depressed continuum could be overcome by referring to the pseudo-continuum, the advantage of CO as the abundance indicator of carbon for M dwarfs outlined above can fully be realized. In fact, we have determined the carbon abundances from CO in 42 M dwarfs rather easily after correcting for the effect of the contamination of numerous weak H_2O lines (section 5). So far, determinations of the elemental abundances in M dwarfs by a direct spectroscopic analysis are rather scarce, and our result for carbon abundances in 42 M dwarfs may be the largest sample of a directly determined elemental abundance or metallicity in M dwarfs at present.

An unsettled problem is that we have two cases of different $T_{\rm eff}$ values for GJ 273 and GJ 725B. As for GJ 725B, the resulting carbon abundance of GJ 725B-H ($\log A_{\rm C}^{(3)} = -3.61 \pm 0.08$) agrees rather well with that of GJ 725A ($\log A_{\rm C}^{(3)} = -3.58 \pm 0.09$) while that of GJ 725B-L ($\log A_{\rm C}^{(3)} = -3.86 \pm 0.08$) does not (see table 10). Although such a test by binary cannot be applied to GJ 273, the result of the binary test for GJ 725B suggests that the $T_{\rm eff}$ by the $M_{3.4}$-method should be preferable for GJ 725B and hence possibly for GJ 273. Also, the deviations from the mean relations in figures $1 \sim 3$ are rather large for GJ 273-L as well as for GJ 725B-L. For these reasons, we adopt the results for GJ 273-H and GJ 725B-H in the following discussion.

We compare our carbon abundances with the metallicities determined from the infrared spectroscopy by Mould (1978) and by Önehag et al. (2012) in table 11 . The error bars were not given explicitly by Mould (1978) and we estimate them to be $\pm$ 0.2 dex from what is mentioned in his text. We also include two representative solar carbon abundances so far proposed, but the values somewhat between these extreme values have also been suggested (e.g., Ayres et al. 2006; Asplund et al. 2009). We plot these data in figure 15a, and our $\log A_{\rm C}$ values show expected positive correlation with [M/H] as a whole. Close inspection of figure 15a reveals that there is bifurcation in the $\log A_{\rm C}$ - [M/H] relation: one branch includes a larger sample of M dwarfs and the Sun with the high carbon abundance (Grevesse et al. 1991) while the other a smaller sample of M dwarfs and the Sun with the low carbon abundance (Allende Prieto et al. 2002).

In table 12, we compare our carbon abundances with the iron abundances determined from the photometric calibrations of [Fe/H] using high resolution spectra (Neves et al. 2013), and plot these data together with the solar values from table 11 in figure 15b. Except for two deviating stars (GJ 406 and GJ 686), the $\log A_{\rm C}$ - [Fe/H] correlation suggests that the C/Fe ratios in M dwarfs are nearly constant at about the solar C/Fe ratio based on the high carbon abundance (Grevesse et al. 1991) rather than on the downward revised carbon abundance (Allende Prieto et al. 2002). This conclusion applies to the majority of M dwarfs shown in figure 15a as well. Given that the determination of carbon abundances is rather difficult in late type stars as exemplified by the solar case and that it is rather easy in M dwarfs by the use of CO as noted above, our result on the carbon abundances in M dwarfs provides a strong constraint on the carbon abundances of the disk population in the solar neighborhood.

Presently known data shown in figure 15 suggest a possibility of bifurcation in C/Fe ratio in M dwarfs. The majority of M dwarfs belong to the group of C/Fe ratio with the high solar carbon abundance and the minority belong to another group of C/Fe ratio with the low solar carbon abundance. It may probably not be a serious problem if few M dwarfs belong to the minority group. However, it should be a problem if the Sun belongs to the minority group or the solar C/Fe ratio is atypical for [Fe/H]=0. This problem if the Sun is a typical star with respect to the relative abundances of the elements at [Fe/H]=0 was examined in detail by the analysis of 189 nearby unevolved stars by Edvardsson et al. (1993), who concluded that the Sun is a quite typical star with respect to the relative abundances of about a dozen of the elements for its metallicity, age, and galactic orbit, although carbon itself was not included in their analysis. We point out that the recent downward revised solar carbon abundance is

[9] In sufficiently low temperatures, say $T \lesssim 4000$ K at $\log P_{\rm g} \approx 6.0$, CO formation is complete and the partial pressure of CO, $P_{\rm CO} \approx A_{\rm C} P_{\rm g}$, is almost independent of T. In the region where CO formation is incomplete (i.e., $P_{\rm CO} << A_{\rm C} P_{\rm g}$), the partial pressures of free C and O are $P_{\rm C} \approx A_{\rm C} P_{\rm g}$ and $P_{\rm O} \approx A_{\rm O} P_{\rm g}$, respectively. Then, $P_{\rm CO} = P_{\rm C} P_{\rm O} / K_{\rm CO}(T) \propto A_{\rm C} A_{\rm O} P_{\rm g}^2 10^{\frac{5040}{T} D_{\rm CO}}$ where $K_{\rm CO}(T)$ is the equilibrium constant defined in Herzberg (1945) and, with the large dissociation energy of CO, $D_{\rm CO} = 11.09$ eV, $P_{\rm CO}$ shows a drastic change with T.

apparently contradicting with this result.

Finally, the distribution of 42 M dwarfs against the carbon abundances is shown in figure 16, and most M dwarfs are confined to the range of $\log A_{\rm C}$ between -3.7 and -3.2 except for few cases outside of this range. Also, our sample includes ten planet hosting M dwarfs (those marked by ‡ in table 1) as illustrated in figure 16. It appears that the planet hosting M dwarfs are biased towards carbon rich side while M dwarfs as a whole towards carbon poor side. As a result, the fraction of the planet hosting M dwarfs is larger in M dwarfs of higher carbon abundances for our present sample. This result is in agreement with a tendency of metallicity in G, F, K, and M stars (e.g., Fischer & Valenti 2005; Johnson & Apps 2009). However, our sample cannot be regarded as an unbiased sample yet and we defer a detailed discussion on this matter to a future paper hopefully on an extended sample of M dwarfs.

---

figure 15a,b: Carbon abundances and metallicities in M dwarfs (p.22).

figure 16: Distribution of carbon abundances in 42 M dwarfs (p.23).

table 11: Carbon abundances and metallicities in M dwarfs (p.32).

table 12: Carbon and iron abundances in M dwarfs (p.32).

6.3. Accuracy of the Abundance Analysis

The major problem in the spectral analysis of cool stars is generally thought to be due to the difficulty to locate the continuum level. We have examined the effect of depressed continuum due to the H_2O veil opacity by our BS analysis and compared with the BB analysis disregarding the effect of H_2O contamination. We have found that the neglect of the H_2O blending results in an error of about 0.1 dex at the largest in the derived abundance (see $\Delta \log A_{\rm C}^{(3)}$ in table 10). The probable errors of the BB analysis are 0.05 - 0.1 dex (table 8) and those of the BS analysis are slightly larger (table 10). Thus, the effect of the depressed continuum may not be very large in the case we have studied in this paper.

We estimate the external errors due to the uncertainties in the fundamental stellar parameters by the BB analysis (subsection 4.3), and the results may be the same for the BS analysis, since the effects of the fundamental parameters should not be different for the two analyses. The uncertainties in $\log g$ and in $\xi_{\rm micro}$ result in rather large external errors in general. However, we used the specified model for the $\log g$ of each M dwarf and we hope that the effect of uncertainty in $\log g$ can be minimized. The problem is the uncertainty in $\xi_{\rm micro}$: If the results of $\xi_{\rm micro} = 0.83 \sim 0.94\,{\rm km\,sec^{-1}}$ (Bean et al. 2006) are typical values for M dwarfs, the uncertainty may not be so large as assumed in subsection 4.3. Anyhow, this is the largest problem in our present analysis and we hope to determine $\xi_{\rm micro}$ by higher resolution spectra in future.

We assume simple one-dimensional LTE models throughout this paper. Certainly, this is an oversimplification to the real photospheres of M dwarfs. For example, convection penetrates to the line forming region even in the classical convective models based on the mixing-length theory (e.g., Tsuji 2002). However, even if inhomogeneity due to convection appears, the CO abundance suffers little change since CO is well stabilized in the photospheres of M dwarfs. For this reason, the inhomogeneity will not have such a drastic effect as in the Sun (e.g., Allende Prieto et al. 2002), at least for the analysis of CO lines in M dwarfs. Also, line formation in the dense photospheres of M dwarfs can be treated within the framework of LTE, especially for the ro-vibration transitions (Hinkle & Lambert 1975).

Finally, we first wondered if abundance analysis could be done with the resolution as low as 20000. We have found, however, that the abundance analysis is rather simple at such a medium resolution, as can be known from the fact that the synthetic spectra can be matched rather easily without specifying any velocity parameters to the observed spectra in which all the details are smeared out by the slit function of FWHM = 16 km sec^{-1}. Such a fitting does not provide any new information except for confirming the abundance determined by the analysis of the EWs, but such a simplicity of analysis will be useful if we are to analyze a large sample of stars. We are convinced that the abundance analysis can be carried out by an analysis of EWs with the spectra of medium resolution, even though a high accuracy as realized by the higher resolution (e.g. $R \gtrsim 50000$) cannot be achieved. However, even if the highest accuracy cannot be attained, the chemical composition is the prime fundamental data in astronomy and should best be determined by the direct analysis of the spectra. We believe that the spectroscopic analysis of M dwarfs can provide unique contribution to the problem of the cosmic chemical abundances and we hope more efforts will be directed to this field.

6.4. Hertzsprung-Russell Diagram at the End of the Main Sequence

The $M_{3.4} - \log T_{\rm eff}$ diagram shown in figure 1 reveals a characteristic feature in that it shows bendings at $\log T_{\rm eff} \approx 3.56$ and ≈ 3.5. Such features should reflect the intrinsic properties of the stellar evolutionary models and, to clarify such a relationship, we generate an $M_{\rm bol} - \log T_{\rm eff}$ diagram or HR diagram by the use of the data given in tables 3 and 4. The result is shown in figure 17 where data based on the interferometry (filled circles) are extended to the lower temperatures by the data based on the infrared flux method (open circles). For comparison, the theoretical HR diagram based on the evolutionary models by Baraffe et al. (1998) is shown by the solid line, on which stellar masses (in unit of $M_\odot$) of the models are indicated. Their models assumed the solar metallicity and covered the range between 0.075 and 1.0 $M_\odot$, thus reaching the very end of the main sequence. Although the number of data points is rather small, observations also cover the same range. The agreement between the theory and observations is fine especially in the regime of

M dwarfs including the coolest ones.

The bendings noted on figure 1 are clearly transformed from those in figure 17. The changes of the slopes in figures 1 and 17 correspond nicely to those in the central temperature - effective temperature relation given in Fig. 1 of Baraffe et al. (1998). These changes of the slope have been explained as due to the onset of convection induced by the H_2 formation in the photospheres of $\approx 0.5\,M_\odot$ dwarfs ($T_{\rm eff} \approx 3600\,$K) and increased importance of the electron degeneracy in the interior of $\approx 0.2\,M_\odot$ dwarfs ($T_{\rm eff} \approx 3200\,$K) (Baraffe et al. 1998). These points roughly correspond to the bendings at $\log T_{\rm eff} \approx 3.56$ and at $\log T_{\rm eff} \approx 3.5$ in figures 17 as well as in figure 1. Thus, recent observational HR diagram reaching the bottom of the main sequence finally provides fine confirmation on the detailed structures of the sophisticated evolutionary models of low mass stars, which had been accomplished long time ago.

figure 17: Observed and theoretical HR diagrams for low mass stars (p.23).

7. Concluding Remarks

In this paper, we have shown that the pseudo-continuum can be evaluated accurately on the theoretical spectrum of the M dwarf and use it as a reference in comparison with the observed spectrum for which only the pseudo-continuum can be known. Then quantitative analysis of the spectra badly depressed by the molecular veil opacities can be carried out to some extent. Such an analysis could be made possible by the recent progress in molecular physics which provided extensive line-lists with high precision (e.g., Barber et al. 2006; Rothman et al. 2010), and the importance of the molecular databases should be emphasized again.

Given that the difficulty due to depressed continuum has been overcome, abundance analysis of M dwarf stars offers unique opportunity which is not realized in other spectral types. In particular, we are now convinced that at least the carbon abundances in late-type stars could best be determined in M dwarfs rather than in solar type stars by the use of CO as the abundance indicator. This result may be somewhat unexpected, but this is due to a favorable circumstance that carbon atoms in M dwarfs are mostly in stable CO molecules which remains almost unchanged for the changes of physical condition in the photospheres of M dwarfs. The similar favorable condition is realized in the determination of oxygen abundance by the analysis of H_2O consuming most oxygen left after CO formation and hence stable in the photospheres of M dwarfs. The accurate determination of carbon and oxygen abundances in M dwarf stars, representing those of the stellar components of the Galactic disk, has a special interest in connection with the yet unsettled problem of the solar carbon and oxygen abundances.

In this work, we mainly observed M dwarfs earlier than dM5 except for dM6.5 dwarf GJ 406, since we thought that it might be difficult to analyze later M dwarfs. However, we find that the dM6.5 dwarf GJ 406 could be analyzed in the same way as in the earlier M dwarfs without any additional problem. Thus we are now convinced that the late M dwarfs can also be analyzed similarly only if the pseudo-continuum level can be defined. In the coolest M dwarfs of $T_{\rm eff} \lesssim 2600\,$K, a new problem is that dust should form in their photospheres (e.g., Tsuji et al. 1996: Jones & Tsuji 1997). We are prepared to extend our analysis to such a case with our Unified Cloudy Models (UCMs) accommodating the dust clouds formed in their photospheres (Tsuji 2002; 2005). We hope that such an extension to the coolest M dwarfs will be a pilot study for future works on more dusty objects including the exoplanets themselves.

Finally, we regret that our analysis is not yet satisfactory in that the spectral resolution ($R \approx 20000$ or velocity resolution of $16\,{\rm km\,sec^{-1}}$) is not high enough to extract the basic information coded in the spectra of M dwarfs (e.g., turbulent velocities) and we hope further progress in high resolution infrared spectroscopy in the near future. The scientific justification for such a quest is obvious. In fact, there are large fields unexplored by high resolution in low luminosity objects including M subdwarfs, dwarf carbon stars, L, T, and Y dwarfs, and exoplanets of various kinds, even if we confine our attention to the objects somewhat related to M dwarfs. The high resolution spectroscopy on these objects will be within the capability of the large telescopes both on ground and in space under planning (or already in construction) only if efficient spectrographs can be developed.

We thank Y. Takeda and the staff of the Subaru Telescope for their help in observations. We also thank Y. Takeda for his help in data reduction of the echelle spectra.

We thank an anonymous referee for careful reading of the text and for helpful suggestions, especially for suggesting to comment on the reason for the bendings in the plot of figure 1.

This research makes use of data products from the Wide-field Infrared Survey Explorer which is a joint project of the University of California, Los Angeles, and the Jet Propulsion Laboratory / California Institute of Technology, funded by NASA.

This research has made use of the VizieR catalogue access tool and the SIMBAD database, both operated at CDS, Strasbourg, France, and of the RECONS database in www.recons.org.

Computations are carried out on common use data analysis computer system at the Astronomy Data Center, ADC, of the National Astronomical Observatory of Japan.

Appendix 1. On the New Effective Temperatures by Interferometry

During the preparation of this manuscript, we notice a paper by von Braun et al. (2014) who reported new measurements of stellar diameters by interferometry, and we find that the effective temperatures of three M dwarfs included in our sample have been determined anew by their work. We compare their results with ours based on the $M_{3.4}$ - $\log T_{\rm eff}$ relation in table 13.

We are a bit shocked to find a large discrepancy for GJ 876, but we are also worried to find that the $T_{\rm eff}$ of this object by the interferometry deviates from the mean relation in figure 1 as the case of GJ 725B. In fact, the situation of GJ 876 is very similar to the case of GJ 725B for which interferometry gave $T_{\rm eff} = 3104\,{\rm K}$ while the $M_{3.4}$-method suggests $T_{\rm eff} = 3337\,{\rm K}$, and we finally decide to adopt the higher value based on the $M_{3.4}$-method by considering the result of a binary test (see subsection 6.2). Presently, we have no solution for GJ 876 and we leave this problem open.

table 13: New $T_{\rm eff}$'s by the interferometry (p.32).

References

Allende Prieto, C., Lambert, D. L. & Asplund, M. 2002, ApJ, 573, L137
Anders, E., & Grevesse, N. 1989, Geochim. Cosmochim. Acta, 53, 197
Apps, K. et al. 2010, PASP, 122, 156
Asplund, M., Grevesse, N., Sauval, A. J., Allende Prieto, C., & Blomme, R. 2005, A&A, 431, 693
Asplund, M., Grevesse, N., Sauval, A. J., & Scott, P. 2009, ARA&A, 47, 481
Avenhaus, H., Schmid, H. M., & Meyer, M. R. 2012, A&A, 548, A105
Ayres, T. R., Plymate, C., & Keller, C. U. 2006, ApJS, 165, 618
Baraffe, I., Chabrier, G., Allard, F., & Hausschildt, P. H. 1998, A&A, 337, 403
Barber, R. J., Tennyson, J., Harris, G. J., & Tolchenov, R. N. 2006, MNRAS, 368, 1087
Bean, J. L., Sneden, C., Hauschildt, P. H., Johns-Krull, C. M., & Benedit, G. F. 2006, ApJ, 652, 1604
Blackwell, D. E., Petford, A. D., & Shallis, M. J. 1980, A&A, 82, 249
Bonfils, X. et al. 2005, A&A, 443, L15
Boyajian, T. S. et al. 2012, ApJ, 757, 112
Butler, R. P., Johnson, J. A.. Marcy, G. W., Wright, J. T., Vogt, S. S., & Fischer, D. A. 2006, PASP, 118, 1685
Butler, R. P., Vogt, S. S. ,Marcy, G. W., Fischer, D. A. Wright, J. T.,Henry, G. W., Laughlin, G., & Lissauer, J. J. 2004, ApJ, 617, 580
Chackerian, C., Jr., & Tipping, R. H. 1983, J. Mol. Spectros., 99, 431
Delfosse, X., Forveille, T., Mayor, M., Perrier, C.,Naef, D., & Queloz, D. 1998, A&A, 338, L67
Delfosse, X., Forveille, T., Ségransam, D., Beuzit, J.-L, Udry, S., Perrier, C., & Mayor, M. 2000, A&A, 364, 217
Edvardsson, B., Andersen, J., Gustafsson, B., Lambert, D. L., Nissen, P. E., & Tomkin, J. 1993, A&A, 275, 101
Faure, A., Wiesenfeld, L., Drouin, B. J., & Tennyson, J. 2013, JQSRT, 116, 79
Fischer, D. A., & Valenti, J. A. 2005, ApJ, 622, 1102
Forveille, T. et al. 2009, A&A, 493, 645
Forveille, T. et al. 2011, A&A, 526, A141
Gezari, D. Y., Schmitz, M., & Mead, J. M. 1987, Catalog of Infrared Observations, Part I, NASA Ref. Pub. 1196
Gliese, W., & Jahreiss, H. 1991, Preliminary Version of the Third Catalogue of Nearby Stars, NASA/Astronomical Data Center, Greenbelt, MD
Grevesse, N., Lambert, D. L., Sauval, A. J., van Dishoeck, E. F., Farmer, C. B., & Norton, R. H. 1991, A&A, 242, 488
Guelachivili, G., De Villeneuve, D., Farrenq, R., Urban, W., & Verges, J. 1983, J. Mol. Spectros., 98, 64
Haghighipour, N., Vogt, S. S., Butler, R. P., Rivera, E. J., Laughlin, G., Meschiari, S., & Henry, G. W. 2010, ApJ, 715, 271
Herzberg, G. 1945, Molecular Spectra and Molecular Structure II. Infrared and Raman Spectra of Polyatomic Moleules (D. Van Nostrand Co. Inc.), p. 526
Hinkle, K. H., & Lambert, D. L. 1975, MNRAS, 170, 447
Howard, A. W. et al. 2010, ApJ, 721, 1467
Johnson, J. A., & Apps, K. 2009, ApJ, 699, 933
Johnson, J. A., Howard, A. W., Marcy, G. W., Bowler, B. P., Henry, G. W., Fischer, D. A., Apps, K., Isaacson, H., & Wright, J. T. 2010, PASP, 122, 149
Jones, H. R. A., & Tsuji, T. 1997, ApJ, 480, L39
Joy, A. H., & Abt, H. A. 1974, ApJS, 28, 1
Kobayashi, N., et al. 2000, Proc. SPIE, 4008, 1056
Lebzelter, T., et al. 2012, A&A, 547, A108
Marcy, G. W., Butler, R. P., Vogt, S. S., Fischer, D., & Lissauer, J. J. 1998, ApJ, 505, L147
Mould, J. R. 1978, ApJ, 226, 923
Neves, V., Bonfils, X., Santos, N. C., Delfosse, X., Forveille, T., Allard, F., & Udry, S. 2013, A&A, 551, A36
Önehag, A., Heiter, U., Gustafsson, B., Piskunov, N., Plez, B. & Reiners, A. 2012, A&A, 542, A33
Partridge, H., & Schwenke, D. W. 1997, J. Chem. Phys., 106, 4618
Rojas-Ayala, B., Covey, K. R., Muirhead, P. S., & Lloyd, J. P. 2012, ApJ, 748, 93
Rothman, L. S., et al. 2010, JQSRT, 111, 2139; more details are found in http://www.cfa.Harvard.edu/hitran/
Struve, O., & Elvey, C. T. 1934, ApJ, 79, 409
Tsuji, T. 1977, PASJ, 29, 497
Tsuji, T. 2002, ApJ, 575, 264
Tsuji, T. 2005, ApJ, 621, 1033
Tsuji, T. 2008, A&A, 489, 1271
Tsuji, T. 2009, A&A, 504, 543
Tsuji, T., Ohnaka, K., & Aoki, W. 1996, A&A, 305, L1
van Leeuwen, F. 2007, A&A, 474, 653
von Braun, K., et al. 2014, MNRAS, 438, 2413
Wallace, L., & Livingston, W. 1992, An Atlas of a Dark Sunspot Umbral Spectrum in the Infrared from 1970 to 8640 $\rm cm^{-1}$, N. S. O. Technical Report No.92-001, NOAO, Tucson
Wright, E. L., et al. 2010, AJ, 140, 1868

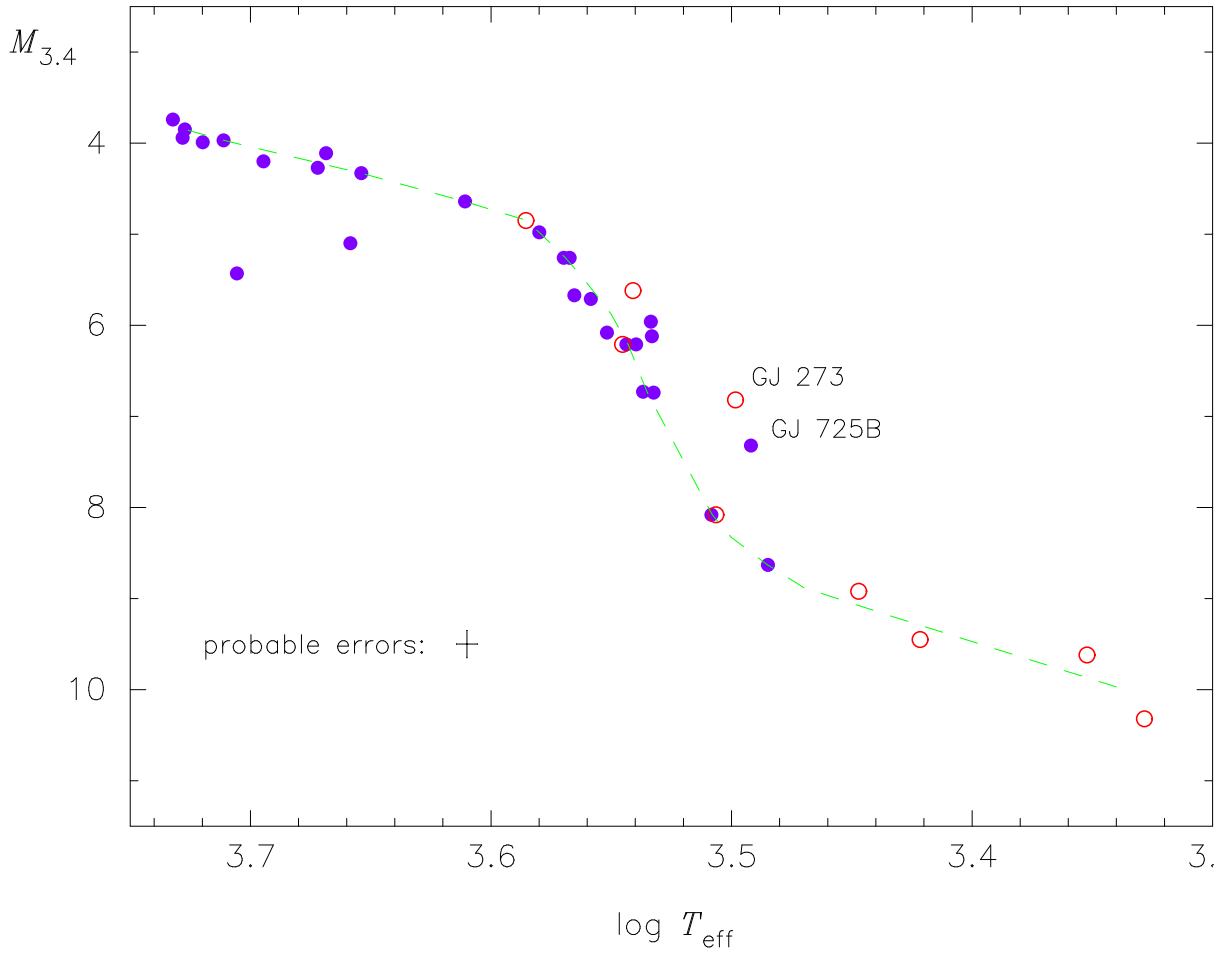

Fig. 1. The absolute magnitude at 3.4 μm, $M_{3.4}$, plotted against $\log T_{\rm eff}$, where $T_{\rm eff}$ values are based on the interferometry (filled circles) and infrared flux method (open circles). The dashed line is a mean curve. The probable errors of $T_{\rm eff}$, reproduced from Table 6 of Boyajian et al. (2012) to our table 3, are less than 1 % for 21 objects out of 27 objects and only one object shows larger than 2 % error in the remainning 6 objects. The probable errors of $M_{3.4}$ are less than 0.15 mag for 22 objects out of 27 objects (see table 3). The error bars representing 1 % probable error in $T_{\rm eff}$ and probable error of 0.15 mag in $M_{3.4}$ are shown at the lower left corner.

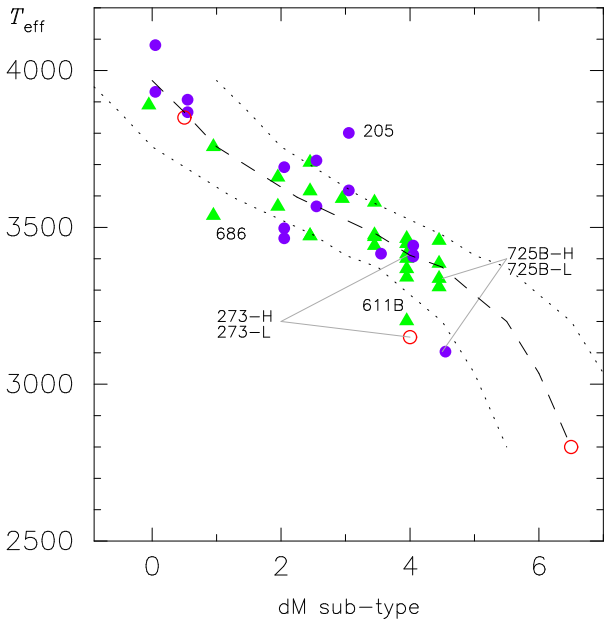

Fig. 2. $T_{\rm eff}$ values based on the interferometry (filled circles), infrared flux method (open circles), and $M_{3.4}$-method (filled triangles) are plotted against sp. types mostly (29 objects) by Joy & Abt (1974) and partly (13 objects) by SIMBAD. Most stars are found within the dispersion of ±1 subtype (dotted lines) around the mean curve (dashed line). The GJ numbers of objects showing large deviations are indicated.

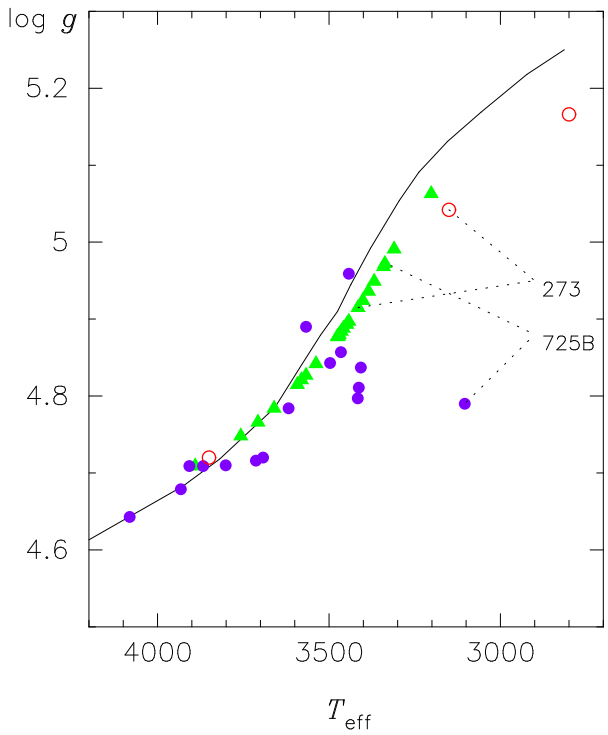

Fig. 3. Log g plotted against $T_{\rm eff}$, where $T_{\rm eff}$ values are based on the interferometry (filled circles), infrared flux method (open circles), and $M_{3.4}$-method (filled triangles). The solid line is based on the evolutionary models by Baraffe et al. (1998).

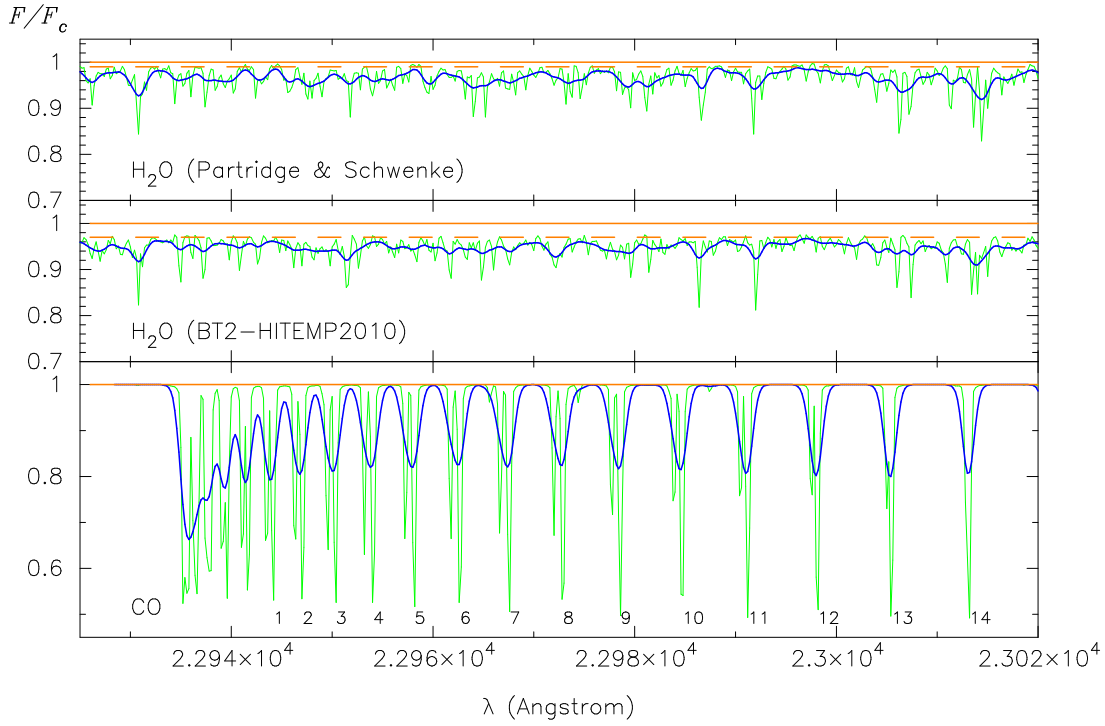

Fig. 4. Theoretical spectra for the model Cc3500c475. The spectra are first calculated with a sampling interval of 0.02 Å(thin lines) and then they are convolved with the slit function of FWHM = 16 km sec^{-1} (thick lines). The true- and pseudo-continuous levels are shown by the solid and dashed lines, respectively. a) H_2O spectrum based on the line-list by Partridge & Schwenke (1997). b) H_2O spectrum based on the line-list BT2-HITEMP2010 (Barber et al. 2006; Rothman et al. 2010). c) CO spectrum near the (2,0) band head. The reference numbers of table 7 are given to respective CO blends.

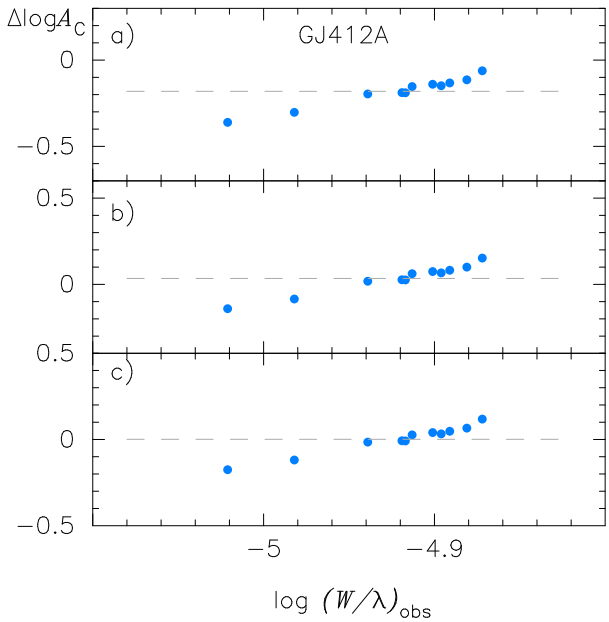

Fig. 5. The resulting logarithmic abundance corrections by the BB analysis for the CO lines in GJ 412A plotted against the observed values of $\log W/\lambda$. The dashed line shows the mean correction. a) First iteration. b) Second iteration. c) Confirmation of the convergence.

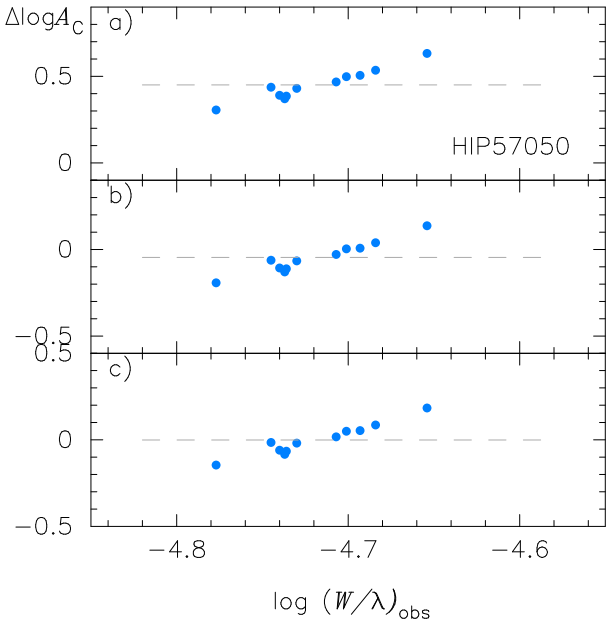

Fig. 6. The resulting logarithmic abundance corrections by the BB analysis for the CO lines in HIP 57050 plotted against the observed values of $\log W/\lambda$. The dashed line shows the mean correction. a) First iteration. b) Second iteration. c) Confirmation of the convergence.

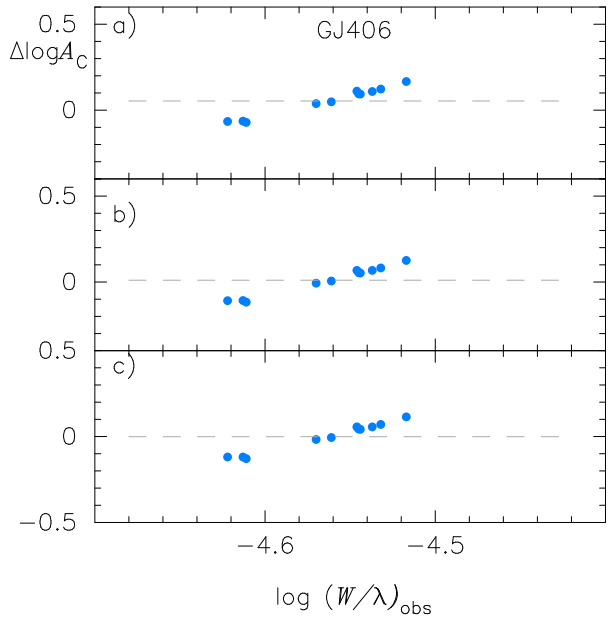

Fig. 7. The resulting logarithmic abundance corrections by the BB analysis for the CO lines in GJ 406 plotted against the observed values of $\log W/\lambda$. The dashed line shows the mean correction. a) First iteration. b) Second iteration. c) Confirmation of the convergence.

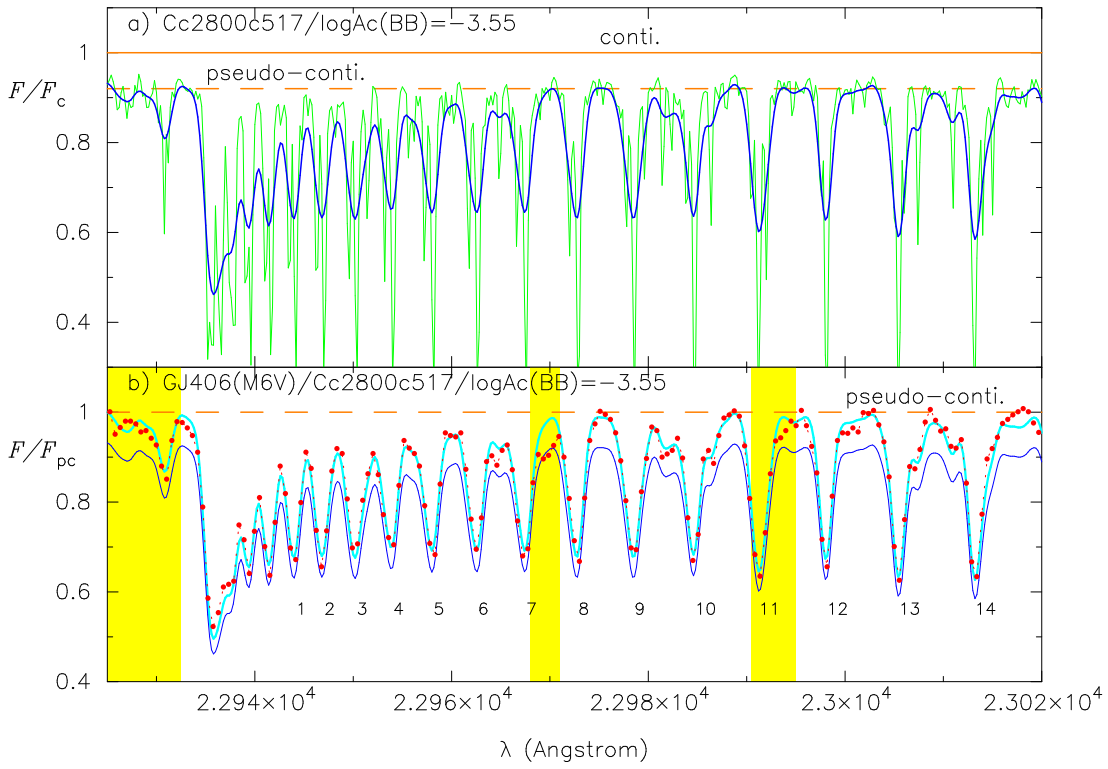

Fig. 8. a) Theoretical spectra for the model Cc2800c517 and with the carbon abundance by the BB analysis, $\log A_{\rm C}^{(2)}$ (table 8) in high (thin line) and low (thick line) resolutions. The continuum level is depressed by about 8 % but the pseudo-continuum level is well defined. b) The theoretical spectrum renormalized by the pseudo-continuum (thick line) can be matched with the observed spectrum of GJ 406 (filled circles), but the theoretical spectrum normalized by the true continuum (copied from figure 8A above but changed to thin line) cannot. The reference numbers of table 7 are given to the respective CO blends.

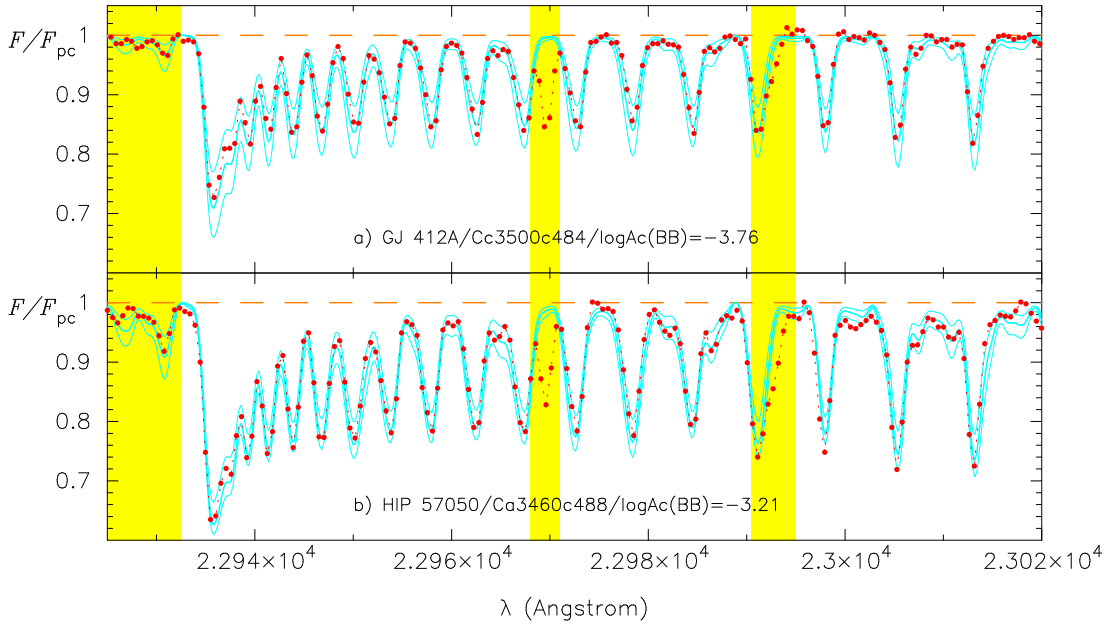

Fig. 9. a) The observed spectrum of GJ 412A (filled circles) is compared with the theoretical one for the model Cc3500c484 (solid lines). The thick line is for the carbon abundance $\log A_{\rm C}^{(2)}$ (table 8) and the thin lines for $\log A_{\rm C}^{(2)} \pm 0.3$. b) The same as a) but for the observed spectrum of HIP 57050 (filled circles) compared with the theoretical one for the model Cc3460c488 (solid lines). Note that all the spectra are normalized by their pseudo-continua.

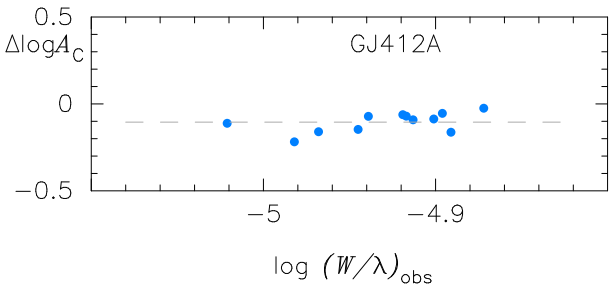

Fig. 10. The resulting logarithmic abundance corrections by the BS analysis for the CO lines in GJ 412A plotted against the observed values of $\log W/\lambda$. The dashed line shows the mean correction.

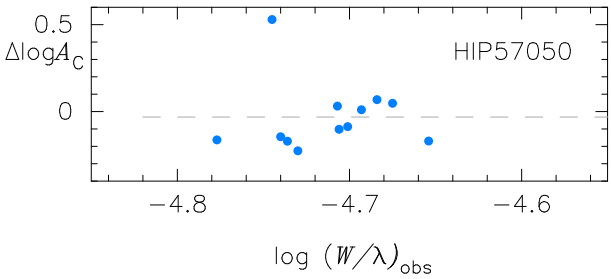

Fig. 11. The resulting logarithmic abundance corrections by the BS analysis for the CO lines in HIP 57050 plotted against the observed values of $\log W/\lambda$. The dashed line shows the mean correction.

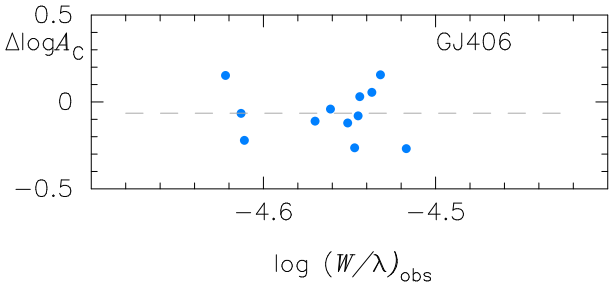

Fig. 12. The resulting logarithmic abundance corrections by the BS analysis for the CO lines in GJ 406 plotted against the observed values of $\log W/\lambda$. The dashed line shows the mean correction.

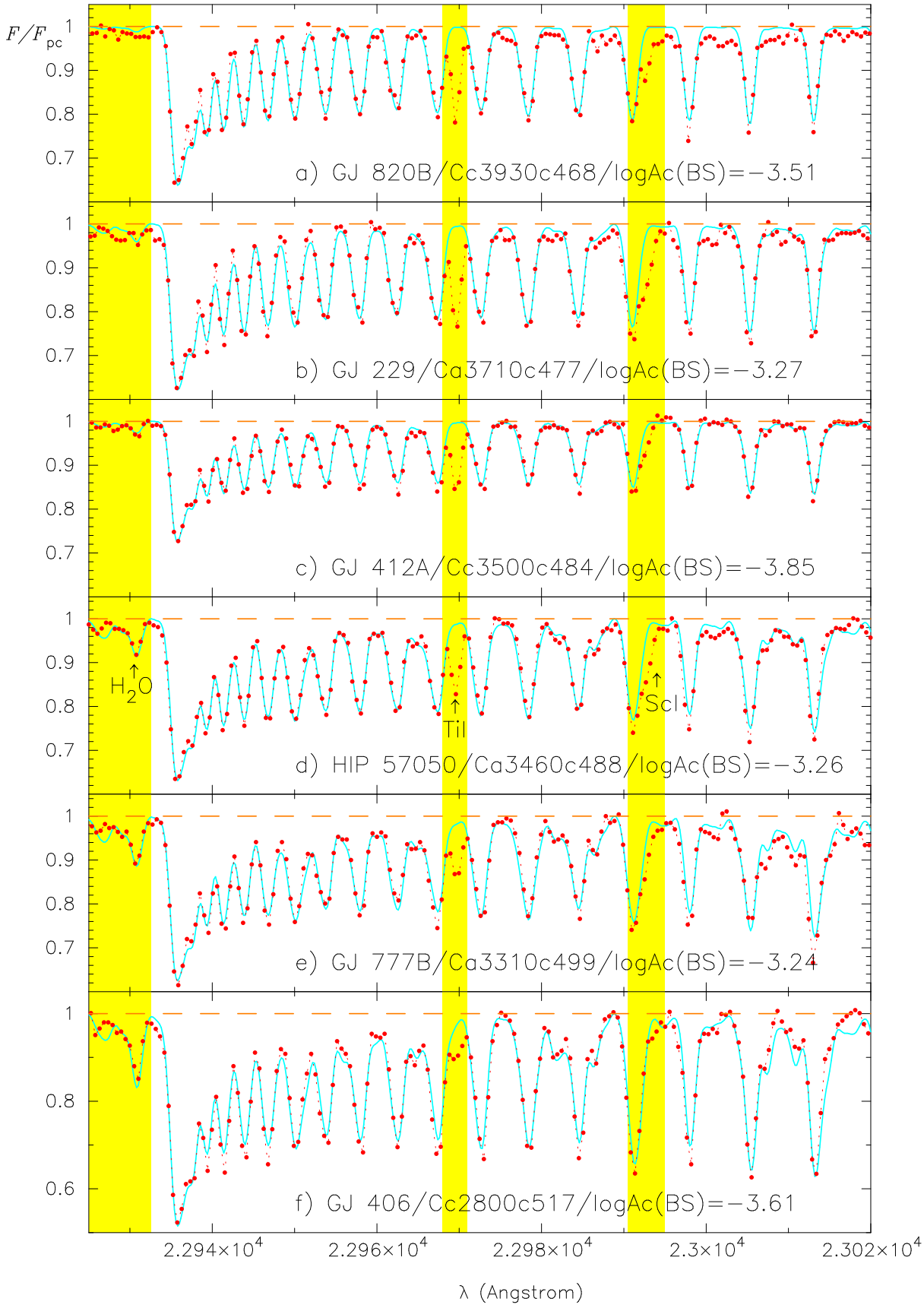

Fig. 13. Comparison of observed (filled circles) and predicted (solid lines) spectra for the carbon abundances by the BS method (table 10) are shown for six M dwarfs: a) GJ 820B (dM0) . b) GJ 229 (dM2.5). c) GJ 412A (dM2). d) HIP 57050 (M4). e) GJ 777B (M4.5). f) GJ 406 (dM6.5e).

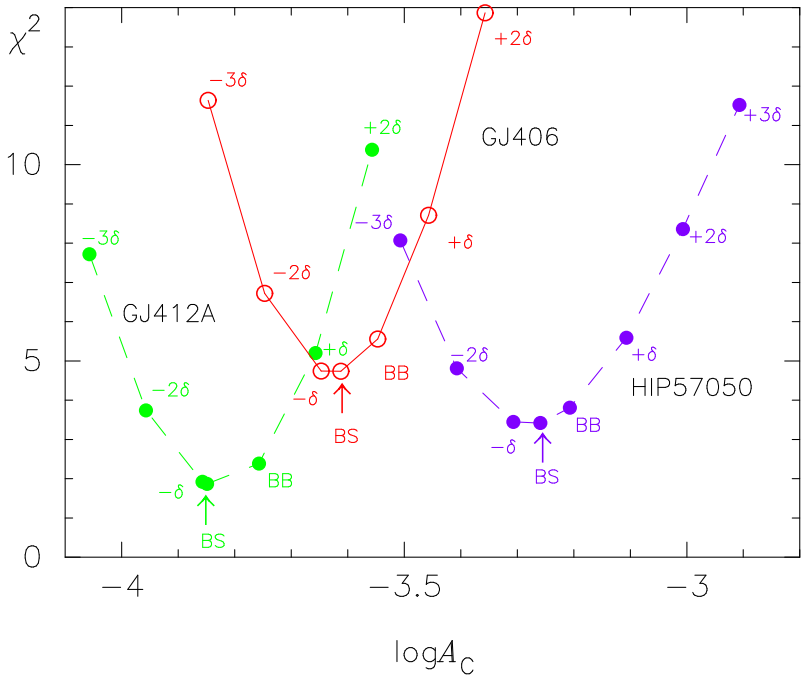

Fig. 14. χ^2 values for the fittings of the observed and predicted spectra are plotted against $\log A_{\rm C}$ for GJ 412A, GJ 406, and HIP 57050. In this figure, BB and BS correspond to the carbon abundances based on BB ($\log A_{\rm C}$(BB)) and BS ($\log A_{\rm C}$(BS)) methods, respectively, and $\pm n\delta$ to $\log A_{\rm C}$(BB) $\pm$ $n\delta$ ($n = 1, 2$, and 3). Note that the results by the BS analysis are almost at the minima but those by the BB analysis are still not.

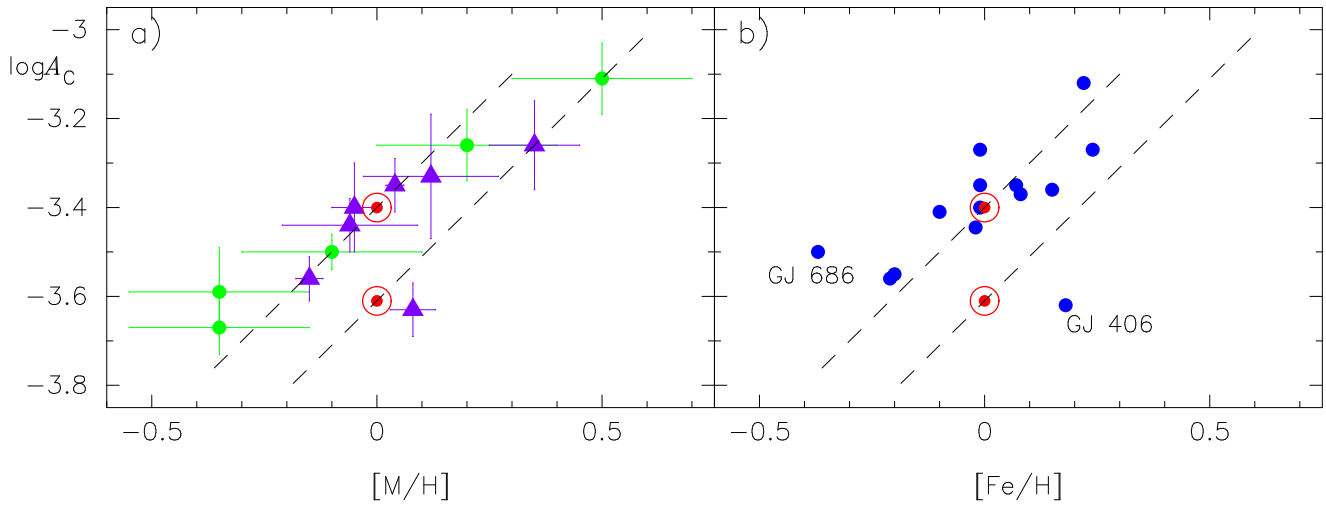

Fig. 15. a) Carbon abundances $\log A_{\rm C}$ (table 10) are compared with the metallicities based on high resolution infrared spectroscopy by Mould (1978) and by Önehag et al. (2012), shown by the filled circles and by filled triangles, respectively. b) Carbon abundances $\log A_{\rm C}$ (table 10) are compared with the [Fe/H] based on the photometric calibrations of [Fe/H] using high resolution spectra by Neves et al. (2013). The upper dashed line represents the locus of C/M (left panel) or of C/Fe (right panel) ratio equal to that with the classical high solar carbon abundance indicated by the upper $\odot$ (Grevesse et al. 1991). The lower dashed line represents the locus of C/M (left panel) or of C/Fe (right panel) ratio equal to that with the recent downward revised solar carbon abundance indicated by the lower $\odot$ (Allende Prieto et al. 2002).

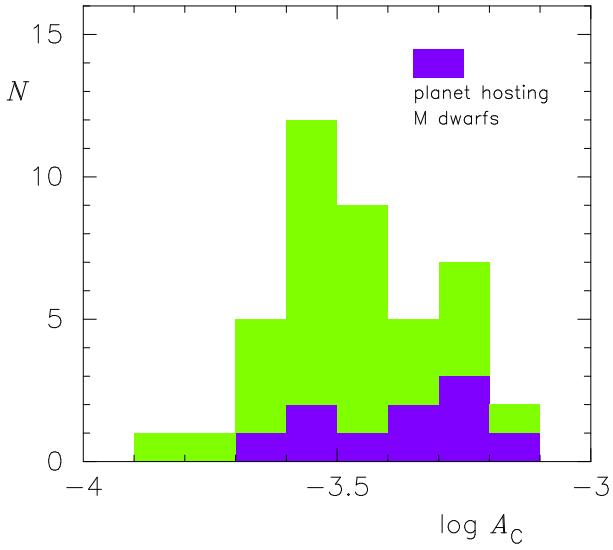

Fig. 16. Frequency distribution of M dwarfs against $\log A_C$. Note that 10 M dwarfs are hosting planet(s).

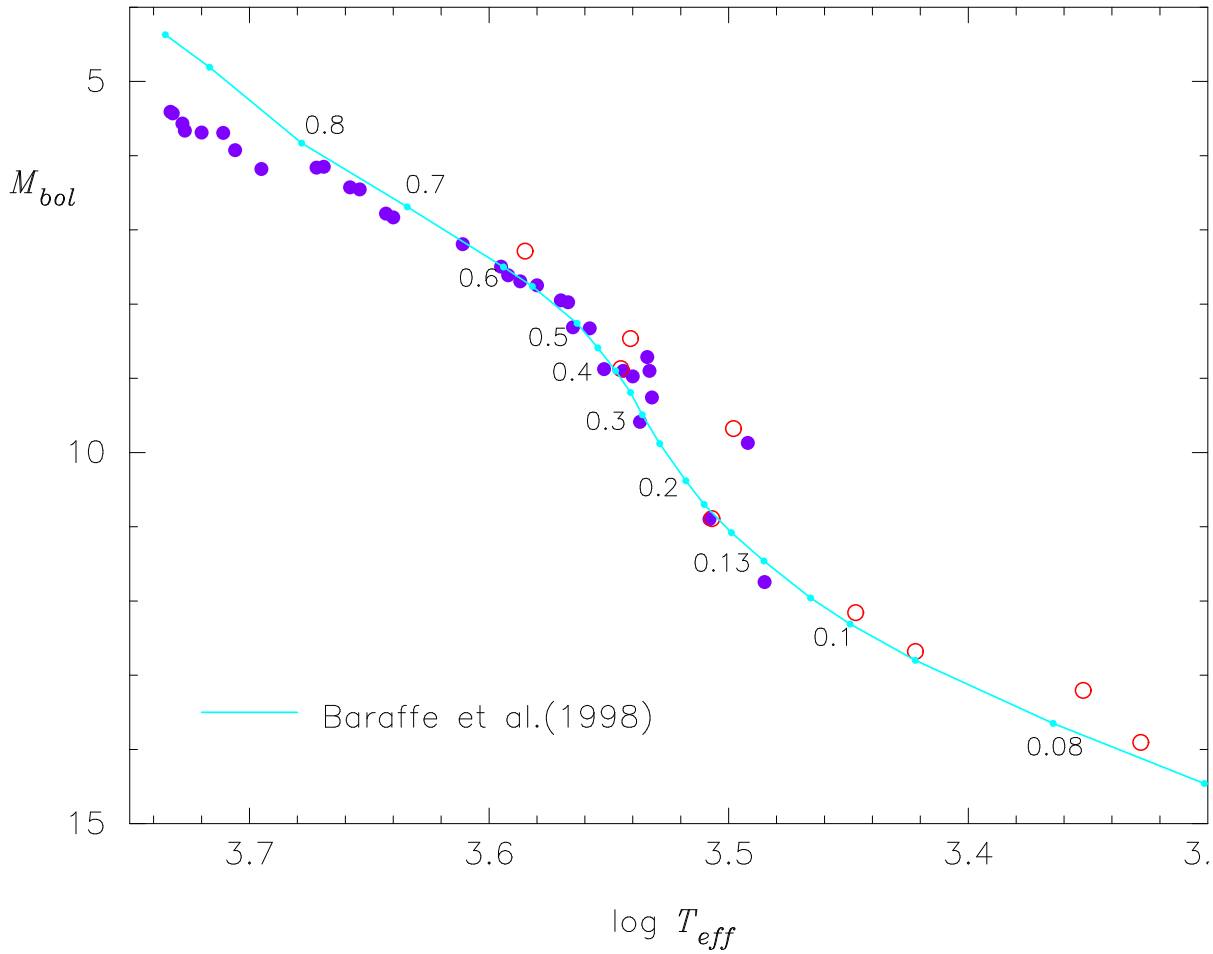

Fig. 17. The absolute bolometric magnitude $M_{\rm bol}$ plotted against $\log T_{\rm eff}$ (HR diagram), where $T_{\rm eff}$ values are based on the interferometry (filled circles) and infrared flux method (open circles) while $M_{\rm bol}$ values from tables 3 and 4. The solid line is based on the evolutionary models of the solar metallicity and the masses of the stellar models are indicated in unit of $M_\odot$ on the curve (as for detail, see Baraffe et al. 1998).

Table 1. Target stars.

GJ/HIP	LHS	Other name	K mag	SNR	Run*
GJ 15A†	3	GX And	4.02	92	Nov
GJ 105B	16	BX Cet	6.57	85	Nov
GJ 166C	25	DY Eri	5.96	93	Nov
GJ 176‡	196	HD 285968	5.61	104	Nov
GJ 179‡		G 83−37	6.94	85	Nov
GJ 205†	30	HD 36395	4.04	89	Nov
GJ 212	1775	HD 233153	5.76	89	Nov
GJ 229	1827	HD 42581	4.17	85	Nov
GJ 231.1B		HD 43587 B	8.27	85	Nov
GJ 250B	1876	HD 50281 B	5.72	76	Nov
GJ 273	33	BD+05 1668	4.86	109	Nov
GJ 324B	2063	ρ Cnc B	7.67	90	Nov
GJ 338A†	260	HD 79210	3.99	112	May
GJ 338B†	261	HD 79211	4.14	114	May
GJ 380†	280	HD 88230	3.26	66	Nov
GJ 406	36	CN Leo	6.08	84	Nov
GJ 411†	37	HD 95735	3.34	114	May
GJ 412A†	38	BD+44 2051	4.77	124	May
GJ 436† ‡	310	G 121−7	6.07	106	May
GJ 526†	47	HD 119850	4.42	127	May
GJ 581† ‡	394	HO Lib	5.84	113	May
GJ 611B	3150	HD 144579 B	9.16	106	May
GJ 649‡	3257	BD+25 3173	5.62	97	May
GJ 686	452	BD+18 3421	5.57	68	Nov
GJ 687†	450	BD+68 732	4.55	114	May
GJ 725A†	58	HD 173739	4.43	95	May
GJ 725B†	59	HD 173740	5.00	113	May
GJ 768.1C		GJ 9671C	8.01	48	May
GJ 777B	3509	HD 190360	8.71	41	May
GJ 783.2B	3530	HD 191785 B	8.88	111	May
GJ 797B NE		G 144−26	8.17	52	May
GJ 797B SW			8.17	52	May
GJ 809†	3595	BD+61 2068	4.62	93	May
GJ 820B†	63	61 Cyg B	2.32	86	Nov
GJ 849‡	517	BD−05 5715	5.59	111	Nov
GJ 876‡	530	IL Aqr	5.01	75	Nov
GJ 880†	533	HD 216899	4.52	94	Nov
GJ 884	3885	HD 217357	4.48	79	Nov
GJ 3348B		HD 35956 B	8.79	38	Nov
HIP 12961‡		CD−23 1056	6.74	70	Nov
HIP 57050‡	2443	GJ 1148	6.82	112	May
HIP 79431‡		LP 804−27	6.59	112	May

* The observing run was either on 2013 May 9 or November 16.
† Angular diameter measured by interferometry.
‡ Planet hosting M dwarf.

Table 2. Echelle setting

Order	Wavelength range (Å)	Dispersion (Å pixel^{-1})
29th	19397−19867	0.460
28th	20089−20575	0.475
27th	20833−21335	0.491
26th	21634−22154	0.508
25th	22500−23039	0.527
24th	23437−23997	0.547
23rd	24456−25038	0.569

Table 3. Fundamental parameters based on $T_{\rm eff}$ by the interferometry

obj.	sp.ty.*	p(msec)†	$F_{3.4}$(mag)‡	$M_{3.4}$(mag)§	$T_{\rm eff}$	$M_{\rm bol}$(mag)‖	$R/R_\odot$	$M/M_\odot$	$\log g$
GJ 15A	dM2.5	278.76 ± 0.77	3.853 ± 0.099	6.08 ± 0.10	3563 ± 11	8.88	0.386	0.423	4.890
GJ 33	K2V	134.14 ± 0.51	3.561 ± 0.142	4.20 ± 0.15	4950 ± 14	6.18			
GJ 53A	G5Vp	132.38 ± 0.82	3.326 ± 0.141	3.94 ± 0.15	5348 ± 26	5.57			
GJ 75	K0V	99.33 ± 0.53	3.753± 0.091	3.74 ± 0.10	5398 ± 75	5.43			
GJ 105	K3V	139.27 ± 0.45	3.395 ± 0.127	4.11 ± 0.13	4662 ± 17	6.15			
GJ 144	K2V	310.94 ± 0.16	2.970 ± 0.251	5.43 ± 0.25	5077 ± 35	5.93			
GJ 166A	K1Ve	200.62± 0.23	2.463± 0.242	3.97 ± 0.24	5143 ± 14	5.69			
GJ 205	dM3	176.77 ± 1.18	3.743 ± 0.120	4.98 ± 0.13	3801 ± 9	7.75	0.574	0.615	4.710
GJ 338A	dM0.5	161.59 ± 5.23			3907 ± 35	7.61	0.577	0.622	4.709
GJ 338B	dM0.5	159.48 ± 6.61			3867 ± 37	7.69	0.567	0.600	4.709
GJ 380	dM0.5	205.21 ± 0.54	3.076 ± 0.149	4.64 ± 0.15	4081 ± 15	7.19	0.642	0.660	4.643
GJ 411	dM2	392.64 ± 0.67	3.239 ± 0.136	6.21 ± 0.14	3465 ± 17	8.97	0.392	0.403	4.857
GJ 412A	dM2	206.27 ± 1.00	4.638 ± 0.085	6.21 ± 0.10	3497 ± 39	8.90	0.398	0.403	4.843
GJ 436	dM3.5	98.61 ± 2.33	5.987 ± 0.052	5.96 ± 0.10	3416 ± 53	8.71	0.455	0.472	4.797
GJ 526	dM3	185.49 ± 1.10	4.372 ± 0.095	5.71 ± 0.11	3618 ± 31	8.33	0.484	0.520	4.784
GJ 551	M5.5V	771.64 ± 2.60	4.195 ± 0.086	8.63 ± 0.09	3054 ± 79	11.74			
GJ 570A	K4V	171.22 ± 0.94	3.159 ± 0.012	4.33 ± 0.02	4507 ± 58	6.46			
GJ 581	dM4	160.91 ± 2.62	5.694 ± 0.055	6.73 ± 0.09	3442 ± 54	9.59	0.299	0.297	4.959
GJ 631	K0V	102.55 ± 0.40	3.797 ± 0.110	3.85 ± 0.12	5337 ± 41	5.66			
GJ 687	dM4	220.84 ± 0.94	4.397 ± 0.094	6.12 ± 0.10	3413 ± 28	8.90	0.418	0.413	4.811
GJ 699	M4V	548.31 ± 1.51	4.386 ± 0.073	8.08 ± 0.08	3224 ± 10	10.90			
GJ 702A	K0VE	196.62 ± 1.38			5407 ± 52	5.41			
GJ 702B	K5Ve	196.62 ± 1.38			4393 ± 149	6.78			
GJ 725A	dM4	280.18 ± 2.18	4.498 ± 0.226	6.74 ± 0.24	3407 ± 15	9.26	0.356	0.318	4.837
GJ 725B-L#	dM4.5	289.48 ± 3.21	5.014 ± 0.325	7.32 ± 0.35	3104 ± 28	9.87	0.323	0.235	4.790
GJ 764	K0V	173.77 ± 0.18	2.786 ± 0.129	3.99 ± 0.13	5246 ± 26	5.69			
GJ 809	dM2	141.87 ± 0.64	4.501 ± 0.088	5.26 ± 0.10	3692 ± 22	7.98	0.547	0.573	4.720
GJ 820A	K5V	287.13 ± 1.51			4361 ± 17	6.83			
GJ 820B	dM0	285.42 ± 0.72			3932 ± 25	7.50	0.601	0.629	4.679
GJ 845	K5V	276.06 ± 0.28	2.899 ± 0.192	5.10 ± 0.19	4555 ± 24				
GJ 880	dM2.5	146.09 ± 1.00	4.432 ± 0.080	5.26 ± 0.09	3713 ± 11	7.95	0.642	0.660	4.643
GJ 887	M0.5V	305.26 ± 0.70	3.243 ± 0.121	5.67 ± 0.13	3676 ± 35	8.31			
GJ 892	K3V	152.76 ± 0.29	3.346 ± 0.098	4.27 ± 0.10	4699 ± 16	6.16			

* The spectral types for M dwarfs we analyze in this paper are by Joy & Abt (1974) and those for other objects from Boyajian et al. (2012).
† Parallax by Hipparcos (van Leeuwen 2007).
‡ *WISE* $W1$ band centered at 3.4 μm (Wright et al. 2010).
§ Absolute magnitude at 3.4 μm.
‖ Absolute bolometric magnitude based on $L/L_\odot$ of Table 6 in Boyajian et al. (2012).
We apply different $T_{\rm eff}$ values - low and high - for this object, and L implies that this is the case of low $T_{\rm eff}$ (see subsection 3.1).

Table 4. Fundamental parameters based on $T_{\rm eff}$ by the infrared flux method

obj.	sp.ty.*	p(msec)†	$F_{3.4}$(mag)‡	$M_{3.4}$(mag)§	$T_{\rm eff}$	$M_{\rm bol}$(mag)‖	$R/R_\odot$	$M/M_\odot$	$\log g$
GJ 273-L#	dM4	262.98 ± 1.39	4.723 ± 0.074	6.82 ± 0.09	3150	9.68	0.141	0.079	5.042
GJ 406**	dM6.5e	419.10 ± 2.10	5.807 ± 0.055	8.92 ± 0.07	2800	12.16	0.139	0.103	5.166
GJ 411***	M2V	392.64 ± 0.67	3.239 ± 0.136	6.21 ± 0.14	3510	8.87			
GJ 644C	M7V	148.92 ± 4.00	8.588 ± 0.023	9.45 ± 0.08	2640	12.68			
GJ 699****	M4V	548.31 ± 1.51	4.386 ± 0.073	8.08 ± 0.08	3210	10.89			
GJ 752A	M3V	170.36 ± 1.00	4.466 ± 0.078	5.62 ± 0.09	3475	8.47			
GJ 752B	M8V	170.36 ± 1.00	8.465 ± 0.023	9.62 ± 0.04	2250	13.21			
GJ 884	dM0.5	121.69 ± 0.69	4.424 ± 0.087	4.85 ± 0.10	3850	7.29	0.551	0.581	4.720
GJ 3849	M9V	95.00 ± 5.70	10.431 ± 0.023	10.32 ± 0.15	2130	13.91			

* The spectral types for M dwarfs we analyze in this paper are by Joy & Abt (1974) and those for other objects from Tsuji et al. (1996).

† Parallax by Hipparcos (van Leeuwen 2007), except for GJ 406 and GJ 644C by RECONS and GJ 3849 by Gliese & Jahreiss (1991).

‡ *WISE W*1 band centered at 3.4 μm (Wright et al. 2010).

§ Absolute magnitude at 3.4 μm.

‖ Absolute bolometric magnitude based on $\log f_{\rm bol}({\rm erg\,cm^{-2}\,sec^{-1}})$ derived by integration of the observed SED in Table 1 of Tsuji et al. (1996) and the parallax.

\# We apply different $T_{\rm eff}$ values - low and high - for this object, and L implies that this is the case of low $T_{\rm eff}$ (see subsection 3.1).

** The empirical formulae by Boyajian et al. (2012) are inapplicable to such a cool M dwarf, and mass is estimated by the use of the mass-luminosity ($M_{\rm K}$) relation by Delfosse et al. (2000) with $K = 6.08$ (Gezari et al. 1987). Radius is inferred from $T_{\rm eff}$ and $L_{\rm bol} = 1.06 \times 10^{-3}\,L_\odot$ based on $M_{\rm bol}$.

*** Compared with $T_{\rm eff}$ = 3465 K by the interferometry (table 3), $T_{\rm eff}$ by the infrared flux method is higher by 45 K.

**** Compared with $T_{\rm eff}$ = 3224 K by the interferometry (table 3), $T_{\rm eff}$ by the infrared flux method is lower by 14 K.

Table 5. Fundamental parameters based on $T_{\rm eff}$ by the $M_{3.4} - \log T_{\rm eff}$ relation (see figure1)

obj.	sp.ty.*	p(msec)†	$F_{3.4}$(mag)‡	$M_{3.4}$(mag)§	$T_{\rm eff}$	$R/R_\odot$	$M/M_\odot$	$\log g$
GJ 105B	dM4.5	129.400 ± 0.000	6.449 ± 0.044	7.01 ± 0.04	3385	0.321	0.325	4.936
GJ 166C	dM4e	198.240 ± 0.000	5.806 ± 0.045	7.29 ± 0.05	3341	0.292	0.288	4.968
GJ 176	dM2.5e	107.830 ± 2.850	5.434 ± 0.066	5.60 ± 0.12	3616	0.454	0.479	4.804
GJ 179	dM3.5e	81.380 ± 4.040	6.785 ± 0.034	6.34 ± 0.14	3476	0.378	0.393	4.877
GJ 212	dM1	80.400 ± 1.690	5.586 ± 0.049	5.11 ± 0.09	3757	0.517	0.546	4.748
GJ 229	dM2.5	173.810 ± 0.990	4.060 ± 0.128	5.26 ± 0.14	3707	0.496	0.524	4.766
GJ 231.1B	M3.5	51.950 ± 0.400	8.044 ± 0.023	6.62 ± 0.04	3442	0.358	0.369	4.897
GJ 250B	M2	114.810 ± 0.440	5.497 ± 0.052	5.80 ± 0.06	3567	0.430	0.452	4.827
GJ 273-H‖	dM4	262.980 ± 1.390	4.723 ± 0.074	6.82 ± 0.09	3415	0.341	0.349	4.915
GJ 324B	M4	76.800 ± 0.000	7.483 ± 0.025	6.91 ± 0.03	3401	0.332	0.337	4.924
GJ 611B	M4	68.870 ± 0.330	8.971 ± 0.023	8.16 ± 0.03	3202	0.185	0.145	5.063
GJ 649	dM2	96.670 ± 1.390	5.502 ± 0.065	5.43 ± 0.10	3660	0.475	0.501	4.784
GJ 686	dM1	123.670 ± 1.610	5.479 ± 0.070	5.94 ± 0.10	3538	0.414	0.434	4.842
GJ 725B-H‖	dM4.5	289.480 ± 3.210	5.014 ± 0.325	7.32 ± 0.35	3337	0.288	0.284	4.972
GJ 768.1C	-	52.110 ± 0.290	7.801 ± 0.026	6.39 ± 0.04	3470	0.375	0.389	4.880
GJ 777B	M4.5	63.060 ± 0.340	8.495 ± 0.024	7.49 ± 0.04	3310	0.269	0.259	4.991
GJ 783.2B	M4	49.040 ± 0.650	8.670 ± 0.022	7.12 ± 0.05	3368	0.310	0.311	4.949
GJ 797B-NE	M2.5	47.740 ± 0.480	7.213 ± 0.027	5.61 ± 0.05	3473	0.377	0.391	4.878
GJ 797B-SW	M2.5	47.740 ± 0.480	7.213 ± 0.027	5.61 ± 0.05	3473	0.377	0.391	4.878
GJ 849	dM3.5	109.940 ± 2.070	5.545 ± 0.056	5.75 ± 0.10	3580	0.436	0.459	4.821
GJ 876	dM4.5	213.280 ± 2.120	4.844 ± 0.077	6.49 ± 0.10	3458	0.368	0.381	4.888
GJ 3348B	M4	39.500 ± 0.000	8.585 ± 0.023	6.57 ± 0.02	3448	0.362	0.373	4.893
HIP 12961	M0	43.450 ± 1.720	6.619 ± 0.039	4.81 ± 0.12	3890	0.565	0.595	4.709
HIP 57050	M4	90.060 ± 2.750	6.665 ± 0.041	6.44 ± 0.11	3464	0.371	0.385	4.884
HIP 79431	M3	69.460 ± 3.120	6.487 ± 0.042	5.70 ± 0.14	3592	0.442	0.466	4.815

* The spectral types beginning with dM are by Joy & Abt (1974) and those beginning with M by SIMBAD.
† Parallax by Hipparcos (van Leeuwen 2007).
‡ *WISE W*1 band centered at 3.4 μm (Wright et al. 2010).
§ Absolute magnitude at 3.4 μm.
‖ We apply different $T_{\rm eff}$ values - low and high - for this object, and H implies that this is the case of high $T_{\rm eff}$ (see subsection 3.1).

Table 6. Effect of the collision partners on the collision half-width for CO pure rotational transitions (see equation 1 as for the definitions of γ_0 and n, under which the collision partner is shown in parenthesis)

$J' - J''$	ν ($\rm cm^{-1}$)	γ_0 ($\rm H_2$)	γ_0 (air)	n ($\rm H_2$)	n (air)
1 - 0	3.845	0.0739	0.0797	0.574	0.76
10 - 9	38.426	0.0721	0.0580	0.628	0.75
20 -19	76.705	0.0700	0.0510	0.603	0.67
30 -29	114.691	0.0681	0.0436	0.594	0.67

Table 7. Spectroscopic data of CO lines (2-0 band)

Ref. no.*	wavelength† (Å)	$\log gf$	L.E.P. (cm^{-1})	Rot. ID.
1	22943.492	-5.130	6289.187	R 57
	22944.160	-5.279	3782.656	R 44
2	22946.312	-5.120	6507.445	R 58
	22947.055	-5.292	3615.553	R 43
3	22949.546	-5.109	6729.297	R 59
	22950.354	-5.305	3452.157	R 42
4	22953.196	-5.099	6954.738	R 60
	22954.055	-5.318	3292.474	R 41
5	22957.262	-5.089	7183.758	R 61
	22958.159	-5.332	3136.510	R 40
6	22961.747	-5.079	7416.348	R 62
	22962.665	-5.345	2984.271	R 39
7	22966.652	-5.069	7652.496	R 63
	22967.572	-5.359	2835.763	R 38
8	22971.977	-5.059	7892.199	R 64
	22972.882	-5.374	2690.992	R 37
9	22977.724	-5.050	8135.441	R 65
	22978.592	-5.388	2549.963	R 36
10	22983.895	-5.040	8382.219	R 66
	22984.704	-5.403	2412.681	R 35
11‡	22990.491	-5.031	8632.520	R 67
	22991.217	-5.418	2279.152	R 34
12	22997.514	-5.021	8886.336	R 68
	22998.131	-5.434	2149.381	R 33
13	23004.965	-5.012	9143.652	R 69
	23005.446	-5.449	2023.372	R 32
14	23012.845	-5.003	9404.465	R 70
	23013.162	-5.466	1901.131	R 31

* Ref. no. refers to figure 4.
† In vacuum.
‡ Blended with Sc I line and not used in our analysis.

Table 8. Carbon abundances in M dwarfs - a preliminary result by the BB method

obj. (1)	$T_{\rm eff}$ (2)	$\log g$ (3)	model 1* (4)	$\Delta\log A_{\rm C}^{(1)\dagger}$ (5)	$\log A_{\rm C}^{(1)}$ (6)	model 2‡ (7)	$\Delta\log A_{\rm C}^{(2)\S}$ (8)	$\log A_{\rm C}^{(2)}$ (9)	$\chi^2_{\rm BB}$ (10)
GJ 15A	3567	4.890	Cc3600c50	0.169	-3.441	Ca3570c489	-0.055	-3.496 ± 0.099	4.381
GJ 105B	3385	4.936	Cc3400c50	0.247	-3.363	Ca3390c494	-0.012	-3.375 ± 0.067	2.820
GJ 166C	3341	4.968	Cc3300c50	0.315	-3.295	Ca3340c497	0.045	-3.250 ± 0.125	4.369
GJ 176	3616	4.804	Cc3600c475	0.339	-3.271	Ca3620c480	0.006	-3.265 ± 0.055	4.285
GJ 179	3476	4.877	Cc3500c50	0.288	-3.322	Ca3480c488	-0.041	-3.363 ± 0.064	3.188
GJ 205	3801	4.710	Cc3800c475	0.594	-3.016	Ca3800c471	-0.050	-3.066 ± 0.042	3.791
GJ 212	3757	4.748	Cc3750c475	0.372	-3.238	Ca3760c475	-0.019	-3.257 ± 0.087	3.330
GJ 229	3707	4.766	Cc3700c475	0.428	-3.182	Ca3710c477	-0.011	-3.193 ± 0.050	3.200
GJ 231.1B	3442	4.897	Cc3400c50	0.111	-3.499	Ca3440c490	-0.002	-3.501 ± 0.044	1.726
GJ 250B	3567	4.827	Cc3550c475	0.214	-3.396	Ca3570c483	0.032	-3.364 ± 0.079	3.234
GJ 273-L	3150	5.040	Cc3200c50	0.101	-3.509	Cc3150c504	-0.049	-3.558 ± 0.048	5.810
GJ 273-H	3415	4.915	Cc3400c50	0.275	-3.335	Ca3420c492	-0.003	-3.338 ± 0.054	4.959
GJ 324B	3401	4.924	Cc3400c50	0.335	-3.275	Ca3400c492	-0.012	-3.287 ± 0.065	5.100
GJ 338A	3907	4.709	Cc3900c475	0.114	-3.496	Ca3910c471	-0.039	-3.535 ± 0.037	2.613
GJ 338B	3867	4.709	Cc3850c475	0.124	-3.486	Ca3870c471	-0.042	-3.528 ± 0.043	2.043
GJ 380	4081	4.643	Cc4100c475	0.470	-3.140	Ca4080c464	-0.071	-3.211 ± 0.085	2.798
GJ 406	2800	5.250	Cc2800c525	0.053	-3.557	Cc2800c517	+0.010	-3.547 ± 0.058	5.558
GJ 411	3465	4.857	Cc3450c475	-0.054	-3.655	Cc3470c486	0.059	-3.605 ± 0.043	2.732
GJ 412A	3497	4.843	Cc3500c475	-0.181	-3.791	Cc3500c484	0.034	-3.757 ± 0.056	4.241
GJ 436	3416	4.797	Cc3400c475	0.047	-3.563	Cc3420c480	0.024	-3.539 ± 0.081	3.991
GJ 526	3618	4.784	Cc3600c475	0.103	-3.507	Cc3620c478	0.018	-3.489 ± 0.041	3.614
GJ 581	3442	4.959	Cc3400c50	0.122	-3.488	Ca3440c496	0.016	-3.472 ± 0.062	2.791
GJ 611B	3202	5.063	Cc3200c50	-0.075	-3.685	Cc3200c506	-0.008	-3.693 ± 0.075	4.315
GJ 649	3660	4.784	Cc3650c475	0.131	-3.479	Ca3660c478	0.005	-3.474 ± 0.053	1.268
GJ 686	3538	4.842	Cc3550c475	0.184	-3.426	Ca3540c484	0.019	-3.407 ± 0.077	3.591
GJ 687	3413	4.811	Cc3400c475	0.259	-3.351	Ca3410c481	0.019	-3.332 ± 0.055	5.592
GJ 725A	3407	4.837	Cc3400c475	0.079	-3.531	Cc3410c484	0.031	-3.500 ± 0.078	3.004
GJ 725B-L	3104	4.790	Cc3100c475	-0.156	-3.766	Cc3100c479	0.004	-3.762 ± 0.098	4.218
GJ 725B-H	3337	4.972	Cc3300c50	0.062	-3.548	Cc3340c497	0.025	-3.523 ± 0.100	3.485
GJ 768.1C	3470	4.880	Cc3500c50	0.249	-3.361	Ca3470c488	-0.045	-3.406 ± 0.092	0.661
GJ 777B	3310	4.991	Cc3300c50	0.348	-3.262	Ca3310c499	0.038	-3.224 ± 0.075	0.827
GJ 783.2B	3368	4.949	Cc3400c50	0.259	-3.351	Ca3370c495	-0.007	-3.358 ± 0.073	4.048
GJ 797B-NE	3473	4.878	Cc3500c50	0.138	-3.472	Ca3470c488	-0.038	-3.510 ± 0.040	1.101
GJ 797B-SW	3473	4.878	Cc3500c50	0.162	-3.448	Ca3470c488	-0.026	-3.474 ± 0.034	1.076
GJ 809	3692	4.720	Cc3700c475	0.159	-3.451	Ca3690c472	-0.033	-3.484 ± 0.058	2.196
GJ 820B	3932	4.679	Cc3950c475	0.200	-3.410	Ca3930c468	-0.056	-3.466 ± 0.036	3.085
GJ 849	3580	4.821	Cc3600c475	0.411	-3.199	Ca3580c482	0.007	-3.192 ± 0.042	5.227
GJ 876	3458	4.888	Cc3500c50	0.408	-3.202	Ca3460c489	-0.045	-3.247 ± 0.045	2.499
GJ 880	3713	4.716	Cc3710c475	0.397	-3.213	Ca3710c472	-0.037	-3.250 ± 0.053	2.990
GJ 884	3850	4.720	Cc3850c475	0.295	-3.315	Ca3850c472	-0.046	-3.361 ± 0.049	2.153
GJ 3348B	3448	4.893	Cc3400c50	0.270	-3.340	Ca3450c489	0.013	-3.327 ± 0.088	0.563
HIP 12961	3890	4.709	Cc3900c475	0.529	-3.081	Ca3890c471	-0.038	-3.119 ± 0.077	2.233
HIP 57050	3464	4.884	Cc3500c50	0.450	-3.160	Ca3460c488	-0.047	-3.207 ± 0.062	3.808
HIP 79431	3592	4.815	Cc3600c475	0.445	-3.165	Ca3590c482	0.009	-3.156 ± 0.080	6.321

* Model photosphere from the UCM grid.

† First correction to the assumed value for the models of the Cc series, $\log A_{\rm C}^{(0)}$ = -3.61.

‡ Specified model for $T_{\rm eff}$ and $\log g$ in the second and third columns, respectively.

§ Second correction to the value in the 6-th column, $\log A_{\rm C}^{(1)}$.

Table 9. Effect of the uncertainties in the fundamental parameters and metallicity on determination of the carbon abundances

obj. ($\log A_{\rm C}^0$)	Ser.	$T_{\rm eff}$ (K)	$\log g$	$\xi_{\rm micro}$ (km sec^{-1})	$\Delta \log A_{\rm C}$	diff.*
GJ 338A	Cc	3900	4.75	1.0	0.039	0.000
(-3.535)	—†	3850	—	—	0.049	0.010
	—	3950	—	—	0.032	-0.007
	—	3900	4.50	—	-0.133	-0.172
	—	—	5.00	—	0.187	0.148
	—	—	4.75	0.5	0.152	0.113
	—	—	—	1.5	-0.075	-0.114
	Ca	—	—	1.0	0.030	-0.009
GJ 436	Cc	3400	4.75	1.0	-0.024	0.000
(-3.539)	—	3350	—	—	-0.051	-0.027
	—	3450	—	—	-0.000	+0.024
	—	3400	4.50	—	-0.116	-0.092
	—	—	5.00	—	0.045	0.069
	—	—	4.75	0.5	0.075	0.099
	—	—	—	1.5	-0.131	-0.107
	Ca	—	—	1.0	-0.023	+0.001
GJ 406	Cc	2800	5.25	1.0	0.000	0.000
(-3.557)	—	2750	—	—	-0.067	-0.067
	—	2850	—	—	0.069	0.069
	—	2800	5.00	—	0.032	0.032
	—	—	5.50	—	-0.031	-0.031
	—	—	5.25	0.5	0.051	0.051
	—	—	—	1.5	-0.065	-0.065
	Ca	—	—	1.0	0.068	0.068
GJ 412A	Cc	3500	4.75	1.0	-0.181	0.000
(-3.61)	Cm‡	—	—	—	-0.275	-0.094

* Difference of $\Delta \log A_{\rm C}$ against that for the reference model in the first line for each star.
† — means identical with the same column of the preceding line.
‡ A metal poor model in which the abundances of all the metals (31 elements) except for He and Li are reduced by 0.20 dex from the abundances of *case c*.

Table 10. Carbon abundances in M dwarfs - a result by the BS method

obj.	$\Delta \log A_{\rm C}^{(3)*}$	$\log A_{\rm C}^{(3)}$	$\chi^2_{\rm BS}$
GJ15A	-0.105	-3.601 ± 0.107	3.660
GJ105B	-0.076	-3.451 ± 0.060	2.864
GJ166C	-0.116	-3.366 ± 0.135	3.812
GJ176	-0.087	-3.352 ± 0.066	3.660
GJ179	-0.064	-3.427 ± 0.114	3.346
GJ205	-0.050	-3.116 ± 0.075	3.728
GJ212	-0.039	-3.296 ± 0.109	3.196
GJ229	-0.078	-3.271 ± 0.074	3.113
GJ231.1B	-0.071	-3.572 ± 0.051	1.674
GJ250B	-0.049	-3.413 ± 0.104	3.054
GJ273-L†	-0.060	-3.618 ± 0.103	5.194
GJ273-H†	-0.065	-3.403 ± 0.109	4.570
GJ324B	-0.068	-3.355 ± 0.121	4.626
GJ338A	-0.052	-3.587 ± 0.035	2.178
GJ338B	-0.050	-3.578 ± 0.035	1.681
GJ380	-0.073	-3.284 ± 0.062	2.828
GJ406	-0.065	-3.612 ± 0.098	4.735
GJ411	-0.066	-3.671 ± 0.055	1.981
GJ412A	-0.092	-3.849 ± 0.036	1.867
GJ436	-0.095	-3.634 ± 0.056	3.391
GJ526	-0.064	-3.553 ± 0.038	2.765
GJ581	-0.088	-3.560 ± 0.049	2.410
GJ611B	-0.069	-3.762 ± 0.034	4.091
GJ649	-0.070	-3.544 ± 0.035	1.140
GJ686	-0.090	-3.497 ± 0.037	3.083
GJ687	-0.096	-3.428 ± 0.091	4.006
GJ725A	-0.084	-3.584 ± 0.092	2.394
GJ725B-L†	-0.096	-3.858 ± 0.076	3.068
GJ725B-H†	-0.082	-3.605 ± 0.079	3.109
GJ768.1C	-0.098	-3.504 ± 0.077	0.573
GJ777B	-0.015	-3.239 ± 0.155	0.827
GJ783.2B	-0.055	-3.413 ± 0.095	3.815
GJ797B-NE	-0.025	-3.535 ± 0.087	1.086
GJ797B-SW	-0.032	-3.506 ± 0.086	1.018
GJ809	-0.066	-3.550 ± 0.044	2.128
GJ820B	-0.040	-3.506 ± 0.045	2.918
GJ849	-0.078	-3.270 ± 0.092	4.217
GJ876	-0.108	-3.355 ± 0.133	2.315
GJ880	-0.098	-3.348 ± 0.067	2.857
GJ884	-0.063	-3.424 ± 0.070	2.024
GJ3348B	-0.079	-3.406 ± 0.108	0.492
HIP12961	-0.069	-3.188 ± 0.070	2.067
HIP57050	-0.052	-3.259 ± 0.122	3.419
HIP79431	-0.080	-3.236 ± 0.116	5.460

* Third correction to the value in the 9-th column of table 8, $\log A_{\rm C}^{(2)}$.

† The cases L and H differ in $T_{\rm eff}$ values (see subsection 3.1), and we finally adopt the carbon abundances of the case H both for GJ 273 and GJ 725B for the reason outlined in subsection 6.2.

Table 11. Carbon abundances and metallicities in M dwarfs

obj.	[M/H]*	$\log A_{\rm C}$§
GJ 15A	-0.35 ± 0.2†	-3.60 ± 0.11
GJ 105B	-0.06 ± 0.15‡	-3.45 ± 0.06
GJ 176	+0.04 ± 0.02‡	-3.35 ± 0.07
GJ 205	+0.5 ± 0.2†	-3.12 ± 0.08
GJ 229	+0.2 ± 0.2†	-3.27 ± 0.07
GJ 250B	-0.05 ± 0.05‡	-3.41 ± 0.10
GJ 411	-0.35 ± 0.2†	-3.67 ± 0.06
GJ 436	+0.08 ± 0.05‡	-3.63 ± 0.06
GJ 581	-0.15 ± 0.03‡	-3.56 ± 0.05
GJ 820B	-0.1 ± 0.2†	-3.51 ± 0.05
GJ 849	+0.35 ± 0.10‡	-3.27 ± 0.09
GJ 876	+0.12 ± 0.15‡	-3.36 ± 0.13
the Sun	0.0	-3.40 ± 0.05‖
the Sun	0.0	-3.61 ± 0.04#

* $[{\rm M/H}] = \log (A_{\rm M})_{*}$- $\log (A_{\rm M})_{\odot}$, where $A_{\rm M}$ is the number density of metal M relative to hydrogen.
† Mould (1978).
‡ Önehag et al. (2012).
§ table 10, this paper.
‖ Grevesse et al. (1991).
Allende Prieto et al. (2002).

Table 12. Carbon and iron abundances in M dwarfs

obj.	[Fe/H]*	$\log A_{\rm C}$†
GJ 105B	-0.02	-3.45
GJ 166C	0.08	-3.37
GJ 176	-0.01	-3.35
GJ 205	0.22	-3.12
GJ 229	-0.01	-3.27
GJ 250B	-0.10	-3.41
GJ 273	-0.01	-3.40
GJ 406	0.18	-3.61
GJ 526	-0.20	-3.55
GJ 581	-0.21	-3.56
GJ 686	-0.37	-3.50
GJ 849	0.24	-3.27
GJ 876	0.15	-3.36
GJ$\dot{8}$80	0.07	-3.35

* Neves et al. (2013).
† table 10, this paper.

Table 13. New effective temperatures by the interferometry

obj.	$T_{\rm eff}$*	$T_{\rm eff}$†	difference
GJ 176	3679 ± 77	3616	+63
GJ 649	3590 ± 45	3660	-70
GJ 876	3129 ± 19	3458	-329

* By interferometry (von Braun et al. 2014).
† By $M_{3.4}$ - $\log T_{\rm eff}$ relation (table 5, this paper).

Table 14. $\log(W/\lambda)_{\rm obs}$* of CO blends (2-0 band) in 42 M dwarfs†–for electronic version only

obj.	no.1	no.2	no.3	no.4	no.5	no.6	no.7	no.8	no.9	no.10	no.12	no.13	no.14
GJ15A	-4.836	-4.926	-4.834	-4.859	-4.855	-4.786	-4.766	-4.749	-4.817	-4.883	-4.887	-4.984	-4.882
GJ105B	-4.756	-4.763	-4.710	-4.738	-4.780	-4.769	-4.718	-4.745	-4.770	-4.831	-4.851	-4.749	-4.676
GJ166C	-4.750	-4.717	-4.653	-4.646	-4.774	-4.683	-4.632	-4.679	-4.704	-4.743	-4.881	-4.734	-4.705
GJ176	-4.747	-4.735	-4.737	-4.757	-4.724	-4.712	-4.710	-4.750	-4.770	-4.723	-4.819	-4.789	-4.808
GJ179	-4.751	-4.764	-4.815	-4.793	-4.803	-4.788	-4.734	-4.722	-4.753	-4.806	-4.776	-4.735	-4.730
GJ205	-4.665	-4.665	-4.653	-4.687	-4.710	-4.652	-4.676	-4.698	-4.690	-4.692	-4.693	-4.698	-4.729
GJ212	-4.734	-4.723	-4.804	-4.771	-4.718	-4.807	-4.712	-4.709	-4.706	-4.761	-4.740	-4.737	-4.754
GJ229	-4.712	-4.718	-4.718	-4.747	-4.759	-4.736	-4.688	-4.707	-4.718	-4.713	-4.743	-4.767	-4.792
GJ231.1B	-4.817	-4.809	-4.773	-4.803	-4.828	-4.851	-4.789	-4.783	-4.819	-4.847	-4.862	-4.788	-4.778
GJ250B	-4.811	-4.786	-4.750	-4.786	-4.788	-4.868	-4.762	-4.745	-4.753	-4.740	-4.783	-4.768	-4.756
GJ273	-4.763	-4.752	-4.727	-4.746	-4.814	-4.781	-4.724	-4.726	-4.744	-4.781	-4.760	-4.726	-4.714
GJ324B	-4.750	-4.744	-4.710	-4.723	-4.748	-4.748	-4.724	-4.661	-4.724	-4.796	-4.758	-4.714	-4.737
GJ338A	-4.810	-4.832	-4.804	-4.838	-4.822	-4.819	-4.785	-4.799	-4.817	-4.842	-4.862	-4.853	-4.934
GJ338B	-4.811	-4.837	-4.803	-4.843	-4.824	-4.815	-4.780	-4.796	-4.818	-4.837	-4.865	-4.852	-4.919
GJ380	-4.640	-4.710	-4.682	-4.703	-4.714	-4.711	-4.662	-4.679	-4.713	-4.687	-4.799	-4.716	-4.799
GJ406	-4.546	-4.570	-4.517	-4.532	-4.561	-4.611	-4.537	-4.544	-4.545	-4.613	-4.622	-4.551	-4.547
GJ411	-4.885	-4.833	-4.811	-4.830	-4.863	-4.881	-4.852	-4.859	-4.863	-4.922	-4.879	-4.848	-4.849
GJ412A	-4.881	-4.896	-4.891	-4.917	-4.919	-4.901	-4.872	-4.913	-4.982	-4.939	-5.021	-4.968	-4.945
GJ436	-4.808	-4.859	-4.768	-4.847	-4.825	-4.806	-4.756	-4.753	-4.802	-4.835	-4.910	-4.839	-4.825
GJ526	-4.829	-4.823	-4.801	-4.832	-4.828	-4.811	-4.776	-4.816	-4.835	-4.814	-4.875	-4.872	-4.840
GJ581	-4.773	-4.799	-4.763	-4.765	-4.824	-4.830	-4.776	-4.809	-4.836	-4.877	-4.889	-4.811	-4.818
GJ611B	-4.886	-4.819	-4.744	-4.831	-4.813	-4.848	-4.820	-4.787	-4.807	-4.893	-4.925	-4.760	-4.738
GJ649	-4.775	-4.803	-4.793	-4.817	-4.848	-4.778	-4.799	-4.821	-4.837	-4.810	-4.897	-4.850	-4.866
GJ686	-4.815	-4.792	-4.700	-4.790	-4.759	-4.792	-4.770	-4.816	-4.775	-	-4.874	-4.803	-4.833
GJ687	-4.754	-4.742	-4.688	-4.696	-4.761	-4.772	-4.712	-4.731	-4.765	-4.750	-4.778	-4.760	-4.744
GJ725A	-4.800	-4.807	-4.736	-4.745	-4.899	-4.790	-4.774	-4.825	-4.837	-4.792	-4.838	-4.776	-4.791
GJ725B	-4.806	-4.803	-4.720	-4.728	-4.851	-4.790	-4.785	-4.803	-4.832	-4.804	-4.967	-4.769	-4.761
GJ768.1B	-4.751	-4.772	-4.719	-4.717	-4.837	-4.794	-4.744	-4.771	-4.821	-4.878	-4.865	-4.768	-4.805
GJ777B	-4.699	-4.686	-4.664	-4.651	-4.719	-4.743	-4.618	-4.702	-4.735	-4.717	-4.752	-4.677	-4.571
GJ783.2B	-4.786	-4.748	-4.690	-4.686	-4.786	-4.762	-4.723	-4.757	-4.782	-4.805	-4.811	-4.678	-4.725
GJ797B-NE	-4.854	-4.814	-4.780	-4.822	-4.836	-4.826	-4.807	-4.807	-4.837	-4.860	-4.824	-4.752	-4.725
GJ797B-SW	-4.844	-4.794	-4.778	-4.792	-4.827	-4.815	-4.807	-4.803	-4.818	-4.826	-4.814	-4.772	-4.709
GJ809	-4.761	-4.788	-4.764	-4.801	-4.862	-4.817	-4.788	-4.797	-4.814	-4.867	-4.841	-4.848	-4.841
GJ820B	-4.802	-4.799	-4.798	-4.794	-4.769	-4.790	-4.766	-4.772	-4.786	-4.788	-4.818	-4.849	-4.826
GJ849	-4.743	-4.690	-4.702	-4.705	-4.714	-4.743	-4.697	-4.724	-4.718	-4.761	-4.745	-4.753	-4.785
GJ876	-4.756	-4.748	-4.712	-4.710	-4.737	-4.727	-4.715	-4.688	-4.743	-4.745	-4.768	-4.863	-4.758
GJ880	-4.697	-4.712	-4.732	-4.741	-4.746	-4.698	-4.728	-4.745	-4.759	-4.711	-4.794	-4.808	-4.817
GJ884	-4.757	-4.744	-4.777	-4.740	-4.805	-4.727	-4.746	-4.753	-4.782	-4.797	-4.793	-4.862	-4.799
GJ3348B	-4.766	-4.743	-4.710	-4.721	-4.755	-4.777	-4.688	-4.745	-4.765	-4.882	-4.793	-4.753	-4.727
HIP12961	-4.719	-4.724	-4.665	-4.648	-4.689	-4.718	-4.649	-4.668	-4.695	-4.742	-4.724	-4.755	-4.789
HIP57050	-4.737	-4.693	-4.654	-4.684	-4.707	-4.736	-4.701	-4.740	-4.730	-4.777	-4.745	-4.675	-4.706
HIP79431	-4.692	-4.695	-4.703	-4.702	-4.698	-4.734	-4.654	-4.693	-4.719	-4.820	-4.730	-4.708	-4.766

* The equivalent widths are measured by referring to the pseudo-continuum.
† The spectroscopic data for lines through no.1 to no.14 are given in table 7 for corresponding Ref. nos.